

Ultrafast dynamics of quantum matter driven by time-energy entangled photons

Giovanni Citeroni,¹ Marco Polini,¹ Michael Dapolito,² D. N. Basov,² and Giacomo Mazza¹

¹*Dipartimento di Fisica dell'Università di Pisa, Largo Bruno Pontecorvo 3, I-56127 Pisa, Italy*

²*Department of Physics, Columbia University, New York, NY, 10027, USA*

We study the dynamics of quantum matter interacting with time-energy entangled photons. We consider the stimulation of a collective mode of a two-dimensional material by means of one of the two partners of a time-energy entangled pair of photons. Using an exactly solvable model, we analyze the out-of-equilibrium properties of both light *and* matter degrees of freedom, and show how entanglement in the incident photons deeply modifies relevant time scales of the light-matter interaction process. We find that entanglement strongly suppresses the delay between the transmission and absorption events, which become synchronous in the limit of strongly entangled wave packets. By comparing numerical simulations with analytic modeling, we trace back this behavior to the representation of entangled wave packets in terms of a superposition of multiple train pulses containing an increasing number of ultrashort non-entangled packets. As a result, we show that the entangled driving allows the creation of a matter excitation on a time scale shorter than the temporal width of the pulse. Eventually, by analyzing temporal correlations of the excited matter degrees of freedom, we show that driving with entangled photons imprints characteristic temporal correlations of time-energy entangled modes in the matter degree of freedom.

I. INTRODUCTION

Light stimulation plays a pivotal role in the investigation of materials properties. It offers unique information on the dynamics of the microscopic degrees of freedom, and, at the same time, it promises tantalizing perspectives for the creation of transient states of matter not achievable in equilibrium conditions [1–5]. Traditionally, light stimulation involves the use of classical pulses with a macroscopically large number of photons. In recent years, the investigation of light-matter interactions involving purely quantum aspects of light have gained a great deal of attention. For example, in the context of quantum materials embedded in optical cavities, the light-matter interaction down to the few-photon or vacuum limits attracted considerable attention [6–28].

Among the unique quantum properties of light, entanglement plays a prominent role for a wide spectrum of applications, ranging from experimental tests of the foundations of quantum mechanics [29, 30] to quantum metrology [31, 32], imaging [33], and the development of quantum technologies [34, 35]. Advancements in quantum light generation stimulated a considerable interest in spectroscopic applications of entangled photons [36–38]. Notable examples include two-photon absorption spectroscopy [39–43], which is an established tool for a broad range of quantum chemistry applications [44–47]. In many cases, entangled photons are generated via spontaneous parametric down conversion (SPDC) mechanisms. These can generate time-energy entangled pairs—see Fig. 1(a)—characterized by a correlation between the frequencies of the two photons [48–52]. Additionally, SPDC-generated pairs can show also polarization entanglement [53, 54]. Time-energy entangled photons are particularly useful in combination with time-resolved spectroscopy techniques [55–58]. For example, they have been exploited in pump-probe experiments, to investigate the dynamics of excited-states [59, 60], and in

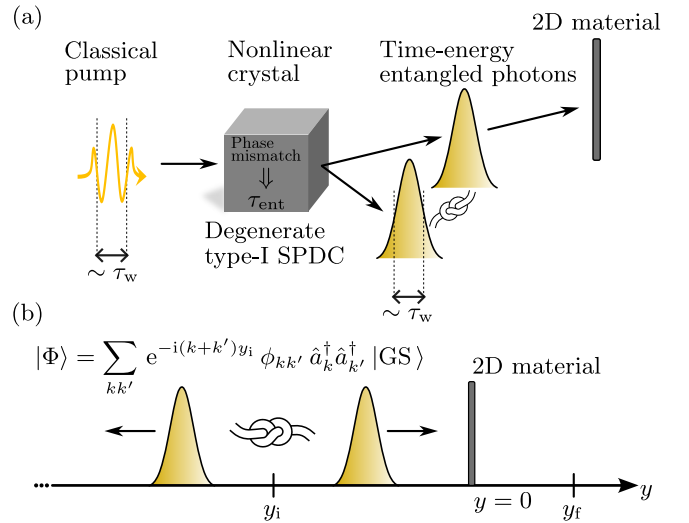


FIG. 1. Panel (a) Sketch of the generation of time-energy entangled photons. A classical pump of temporal width τ_w excites a nonlinear crystal producing two time-energy entangled photons via SPDC. The phase mismatch between the wave-vectors of the classical pulse and the generated pair defines the entanglement time τ_{ent} . The knot represents the entanglement carried by the photon pair. One of the two partners of the entangled photon pair scatters onto a 2D material. Panel (b) Sketch of our theoretical model. The time-energy entangled pair consists of two counter-propagating photon packets moving along the y direction, see Eq. (3). The right-propagating packet interacts with a collective excitation hosted by a 2D material placed at $y = 0$. The symbol y_i [y_f] indicates the position at which the photon pair is created [the transmitted photons are measured].

interferometric setups to measure femtosecond dephasing times using continuous-wave pulses [61].

So far, the theoretical investigation of the effects of the photon entanglement in the light-matter interaction

processes focused, almost exclusively, on the properties of light. For example, spectroscopic signals involving entangled photons have been determined for various setups by means of perturbative methods—see e.g. Ref. [36] for a review. While relevant predictions have been made, these approaches do not generally provide information on the properties of the matter degrees of freedom excited by entangled photons. In this Article, we point out that the understanding of the non-equilibrium dynamics of matter stimulated by entangled light can be of fundamental interest, greatly transcending applications in the context of quantum spectroscopy. In particular, we highlight the fact that matter degrees of freedom are naturally characterized by an intrinsic entanglement, which can potentially be controlled, for example, by classical [62–64] or vacuum fields [65, 66]. Therefore, a deep understanding of the hybridization between entangled photons and matter degrees of freedom represents a fundamental step for opening new frontiers in the exploration of light-matter interactions, and, possibly, guiding the search for exotic light-induced phases of matter.

In this Article, we study an *exactly solvable* model which allows us to describe the dynamics of hybrid light-matter excitations (i.e. polaritons [67, 68]) induced by the stimulation of matter degrees of freedom by time-energy entangled photons. Specifically, we consider a scattering problem in which a single partner of a time-energy entangled photon pair interacts with a resonant (non-dispersive) medium described by a collective matter excitation hosted by a 2D material, see Fig 1(b). By varying the time-energy correlations of the incident photon, we show that entanglement induces qualitative changes in the dynamics of both transmitted photons and light-stimulated matter excitations.

By using incident packets of fixed temporal width, we show how entanglement significantly enhances transmission across the material. The transmission enhancement is characterized by a crossover from delayed to synchronized transmission and absorption peaks occurring, respectively, for weakly and strongly entangled incoming pulses. Focusing on the dynamics of light-stimulated matter excitations, we show that the entangled driving modifies the time scales of energy transfer from the light to the matter degrees of freedom. In particular, we show how energy is absorbed on a time scale shorter than the packet width, thus highlighting how temporally-wide entangled photon packets share some similarities with ultrashort light pulses. We understand these behaviors by showing that an entangled pulse can be represented by a superposition of train of pulses containing an increasing number of shorter and shorter non-entangled packets. Eventually, we show how the polariton dynamics leads to the creation of matter excitations characterized by temporal correlations of time-energy entangled modes

Our Article is organized as following. In Section II we introduce our model and describe the entangled-photon drive considered in this work. In Section III we present our main results. This Section is organized into three

parts. In Sect. III A we discuss the results relative to the dynamics of photon transmission processes through the material and introduce a representation of entangled packets in terms of a superposition of non-entangled train pulses. Section III B contains results concerning the dynamics of the light-stimulated matter excitation, whereas, in Section III C, we discuss the temporal correlations induced by the entangled photon driving. Finally, in Sect. IV we summarize our main findings and draw our conclusions.

II. SETUP AND ENTANGLED PHOTONS

We consider a scattering setup in which a single photon propagating along the y -axis impinges on a 2D material in the x - z plane at $y = 0$, see Fig. 1(b). The incident photon is entangled with another photon which propagates in the opposite direction and does not interact with the material.

We describe entangled photons by populating the modes of the electromagnetic field quantized in a cavity of length L_y [69]. We take the cavity large enough so that, for all practical purposes, we deal with the continuum of free-space electromagnetic modes. Each photon mode is labeled by an in-plane wave-vector \mathbf{q} , an out-of-plane wave-number k , and an associated polarization λ . Here, “out-of-plane” and “in-plane” are referred to the x - z plane of the 2D material.

In this Article, we consider the interaction between light and a single collective mode of the material with zero in-plane wave-vector, $\mathbf{q} = \mathbf{0}$, and polarization along the x -axis, so that our theory includes only photonic modes with $\mathbf{q} = \mathbf{0}$ and a single polarization $\lambda = \hat{x}$. From now on, we drop the dependence on these two indices. We model the collective mode of the matter degrees of freedom as an harmonic oscillator of frequency ω_0 . This mode may represent, for example, a zone-center optical phonon, a 2D gapped plasmon [70–72], an exciton or a magnon in an atomically-thin semiconductor [67, 68]. For the sake of concreteness, we fix the energy of the collective mode at $\hbar\omega_0 = 100$ meV, without further specifying its microscopic origin.

Upon minimal coupling substitution [73, 74], the light-matter Hamiltonian therefore reads as following:

$$\hat{\mathcal{H}} = \hat{\mathcal{H}}_{\text{mat}} + \hat{\mathcal{H}}_{\text{pht}} + \hat{\mathcal{H}}_{\text{mat-pht}}. \quad (1)$$

Here, $\hat{\mathcal{H}}_{\text{mat}} = \hbar\omega_0 \hat{b}^\dagger \hat{b}$ and $\hat{\mathcal{H}}_{\text{pht}} = \sum_k \hbar\omega_k \hat{a}_k^\dagger \hat{a}_k$ with $\omega_k = c|k|$ are, respectively, the bare matter and photon Hamiltonians, where \hat{b} [\hat{b}^\dagger] and \hat{a}_k [\hat{a}_k^\dagger] are the corresponding bosonic annihilation [creation] operators and c is the speed of light in vacuum. The last term in Eq. (1), $\hat{\mathcal{H}}_{\text{mat-pht}} = \hat{\mathcal{H}}_A + \hat{\mathcal{H}}_{A^2}$, represents light-matter interactions and contains paramagnetic and diamagnetic contributions, which read, respectively,

$$\hat{\mathcal{H}}_A = -i\hbar\omega_0 \sum_k \frac{\tilde{g}}{\sqrt{\omega_k}} (\hat{b}^\dagger \hat{a}_k + \hat{b} \hat{a}_k^\dagger) + \text{H.c.}, \quad (2a)$$

$$\hat{\mathcal{H}}_{A^2} = \hbar\omega_0 \sum_{k,k'} \frac{\tilde{g}^2}{\sqrt{\tilde{\omega}_k \tilde{\omega}_{k'}}} (\hat{a}_k^\dagger \hat{a}_{k'} + \hat{a}_k^\dagger \hat{a}_{k'}^\dagger) + \text{H.c.} \quad (2b)$$

Here, $\tilde{\omega}_k \equiv \omega_k/\omega_0$ is the dimensionless photon frequency (i.e. the photon frequency ω_k measured in units of ω_0) and $\tilde{g} \equiv \tilde{q}\sqrt{\alpha\pi c/(L_y\omega_0)}$ is a dimensionless coupling defined by the fine structure constant $\alpha = e^2/(\hbar c) \simeq 1/137$ and the dimensionless effective charge \tilde{q} of the collective mode. Unless specified elsewhere, we set $\tilde{q} = 1$ and introduce a high-energy cut-off $\Lambda = 2\omega_0$ on the photonic modes. All the results presented below are converged with respect to this cutoff.

The Hamiltonian (1) is bilinear in the bosonic annihilation/creation operators and, upon introducing polariton operators [75] $\hat{\gamma}_a$ and $\hat{\gamma}_a^\dagger$, can be brought in diagonal form $\hat{\mathcal{H}} = \sum_a \varepsilon_a \hat{\gamma}_a^\dagger \hat{\gamma}_a$ by a multi-mode canonical para-unitary transformation [76], see Appendix A. The vacuum state of the polaritonic modes, $\hat{\gamma}_a$ and $\hat{\gamma}_a^\dagger$, defines the ground state of the Hamiltonian, i.e. $\hat{\gamma}_a|\text{GS}\rangle = 0$. Notice that, due to the presence of terms of the form $\hat{b}^\dagger \hat{a}_k^\dagger$, $\hat{a}_k^\dagger \hat{a}_{k'}^\dagger$, and Hermitian conjugates in Eqs. (2a) and (2b), the $|\text{GS}\rangle$ does not coincide with the vacuum of bare photon and matter operators $\hat{a}_k|0\rangle = \hat{b}|0\rangle = 0$. As a result, the resonance frequency gets dressed by the light degrees of freedom and undergoes a blue shift $\omega_0 \rightarrow \omega_* \simeq 1.008\omega_0$. Further details about the preparation of the initial state and this blue shift of the matter resonant frequency can be found in Appendix B and C, respectively.

Starting from $|\text{GS}\rangle$ at $t = 0$, we suddenly change the state of the system by creating a two-photon Fock state describing counter-propagating packets centered at an initial position $y_i < 0$ on the left side of the material, see Fig. 1. The sudden creation of the two-photon state brings the system out-of-equilibrium and the unitary dynamics governed by the Hamiltonian in Eq. (1) describes the spatio-temporal propagation of the two packets and, in particular, the interaction of the right-moving packet with the material. The $t = 0$ two-photon state reads

$$|\Phi\rangle = \sum_{k>0} \sum_{k'<0} e^{-i(k+k')y_i} \phi_{kk'} \hat{a}_k^\dagger \hat{a}_{k'}^\dagger |\text{GS}\rangle, \quad (3)$$

where the frequency-dependent coefficients, $\phi_{kk'} = \phi(\omega_k, \omega_{k'})$, define the entanglement properties of the two-photon state. In this Article, we consider a time-energy entangled pair in which entanglement is controlled by the correlation between the frequencies of the two counter-propagating packets. Specifically, we consider a simplified version of a type-I SPDC state [73, 74, 77–80] defined by two time scales, τ_w and τ_{ent} as

$$\phi_{kk'} = \mathcal{N}_{\text{ent}} e^{-(\omega_k + \omega_{k'} - 2\omega_0)^2 \tau_w^2} \times \text{sinc}((\omega_k - \omega_0)^2 \tau_{\text{ent}}^2 + (\omega_{k'} - \omega_0)^2 \tau_{\text{ent}}^2), \quad (4)$$

where $\text{sinc}(x) = \sin(x)/x$ and \mathcal{N}_{ent} is a normalization factor such that $\langle \Phi | \Phi \rangle = 1$. The two-photon state in Eq. (3) can be generated by stimulating a birefringent material with a classical pulse. The time scales τ_w and

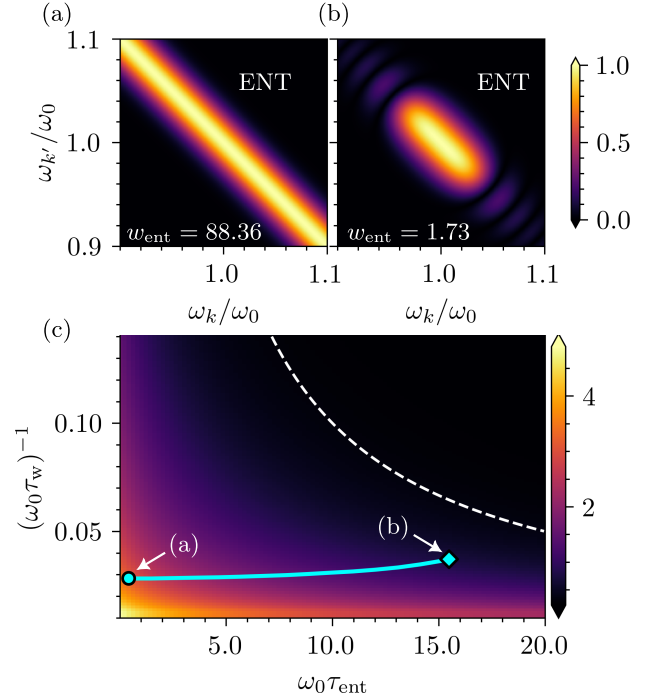


FIG. 2. Panels (a)-(b) Modulus $|\phi_{kk'}|$ of the mode-dependent coefficients $\phi_{kk'}$, see Eq. (4), defining the two-photon entangled state in Eq. (3). The physical meaning of $\phi_{kk'}$ is explained in the main text. The mode-dependent coefficients are normalized to their maximum value. Panel (a) Results for $\tau_w \approx 232.02$ fs and $\tau_{\text{ent}} \approx 2.63$ fs, corresponding to an entanglement parameter $w_{\text{ent}} \approx 88.36$, see Eq. (5). Panel (b) Results for $\tau_w \approx 176.59$ fs and $\tau_{\text{ent}} \approx 101.88$ fs, corresponding to $w_{\text{ent}} \approx 1.73$. Panel (c) The von Neumann entropy is plotted as a function of $(\omega_0 \tau_w)^{-1}$ and $\omega_0 \tau_{\text{ent}}$. The white dashed line corresponds to $w_{\text{ent}} = 1$, where w_{ent} is defined in Eq. (5). States carrying strong entanglement fall below the dashed line. The cyan line represents the locus of points in parameter space for which the entangled packets have a fixed temporal width corresponding to a FWHM of approximately 556 fs. The dot and diamond symbols denote the points corresponding to panels (a) and (b) above.

τ_{ent} are related, respectively, to the width of the pulse, $\sigma_w \sim \tau_w^{-1}$, and the wave-vector mismatch inside the nonlinear crystal [50]. The quantity $\phi_{kk'}$ gives the probability amplitude of measuring two photons with momenta k and k' . We notice from Eq. (4) that the coefficients $\phi_{kk'}$ cannot be factorized, i.e. $\phi_{kk'} \neq \psi_k \psi_{k'}$. As a result, the state $|\Phi\rangle$ cannot be written as a product state of left- and right-moving packets, i.e. $|\Phi\rangle \neq |\Phi_L\rangle |\Phi_R\rangle$, highlighting its entangled nature.

The non-separability of the state is determined by the frequency correlations set by the exponential and sinc factors in Eq. (4) and controlled by the two time scales τ_{ent} and τ_w . In the limit $\tau_{\text{ent}} \ll \tau_w$, the frequencies of the two packets are anti-correlated around the resonance frequency, i.e. $\omega_{k'} \approx 2\omega_0 - \omega_k$, over a broad range of frequencies, see Fig. 2(a). By increasing the parameter

τ_{ent} , the frequencies become anti-correlated on a much smaller frequency range—Fig. 2(b)—implying that, for $\tau_{\text{ent}} \gg \tau_w$, the state evolves towards a separable one, i.e. $|\Phi\rangle \approx |\Phi_L\rangle|\Phi_R\rangle$. We confirm these expectations by direct calculation of the entanglement entropy associated to the partitioning of the photon Hilbert space into two sectors, one corresponding to positive value of the wave-number k and one to negative values of k , representing, respectively, right- and left-moving modes, see Appendix D for details. Panel (c) of Fig. 2 displays the entanglement entropy as a function of $(\omega_0\tau_w)^{-1}$ and $\omega_0\tau_{\text{ent}}$. The entanglement entropy is large for $\tau_w/\tau_{\text{ent}} \gg 1$ while it is strongly suppressed for $\tau_w/\tau_{\text{ent}} \lesssim 1$.

We quantify the temporal widths of the packets by computing their full width at half maximum (FWHM). For the packets defined by Eq. (4), the FWHM is controlled by both time scales τ_w and τ_{ent} . In the following, we have decided to fix the temporal width of the entangled packets and change the two time scales to control the entanglement entropy of the state. Specifically, we introduce the parameter

$$w_{\text{ent}} \equiv \frac{\tau_w}{\tau_{\text{ent}}} \quad (5)$$

and restrict our analysis to the parameter region $w_{\text{ent}} > 1$, see cyan line in Fig. 2(c). Strongly [weakly] entangled packets occur for $w_{\text{ent}} \gg 1$ [$w_{\text{ent}} \gtrsim 1$]. For $w_{\text{ent}} > 1$ it is possible to check that the entangled packets described by Eq. (3) with the choice (4) have a Gaussian shape. Therefore, we compare the results obtained with entangled packets, evaluated at different values of w_{ent} , with those obtained for rigorously separable Gaussian packets defined by

$$\phi_{kk'}^{\text{sep}} = \psi_k \psi_{k'} = \mathcal{N}_{\text{sep}} e^{-(\omega_k - \omega_0)^2 \tau_{\text{sep}}^2} e^{-(\omega_{k'} - \omega_0)^2 \tau_{\text{sep}}^2}. \quad (6)$$

Here, \mathcal{N}_{sep} is a normalization constant and τ_{sep} defines the temporal width of the separable packets. For the separable packets, the FWHM depends only on τ_{sep} .

III. RESULTS

In the following sections we present results obtained by numerically solving the equations of motion for the coupled photon and matter degrees of freedom. As already mentioned above, the Hamiltonian in Eq. (1) can be diagonalized exactly. The corresponding equations of motion therefore describe the exact unitary dynamics of the coupled light-matter system.

We organize the presentation of our results into three parts. Sect. III A and III B are devoted to time-dependent observables of photonic and matter degrees of freedom, respectively. Finally, in Sect. III C, we discuss non-local temporal correlations of both degrees of freedom.

Before presenting our results, it is important to specify some numerical details regarding the system under

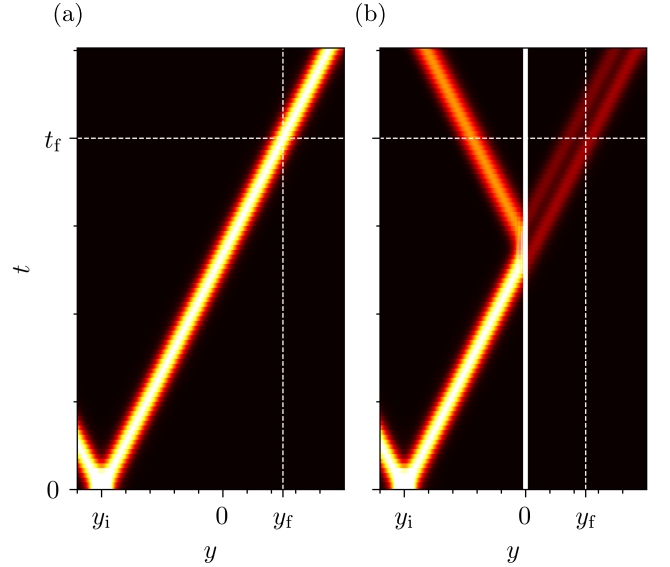


FIG. 3. Spatio-temporal evolution of the photon number density $n_{\text{pht}}(t, y)$, see Eq. (7), of the left- and right-propagating entangled packets created at time $t = 0$ at position y_i . Numerical results in this figure refer to the case of entangled packets with $w_{\text{ent}} = 1.73$. Panel (a) Results for the case of freely-propagating packets. Panel (b) The right-propagating packet interacts with the 2D material at $y = 0$, here represented by a thick white line. In both panels, the evolution of the left-propagating packet is cut for visualization purposes. Vertical [horizontal] dashed lines represent the position y_f where transmitted photons are measured [the time t_f at which the freely propagating packet reaches the position y_f].

consideration. In the setup shown in Fig. 1 (b), periodic boundary conditions (PBCs) are imposed at $y = -\frac{L_y}{2}$ and $y = \frac{L_y}{2}$. The two photon wave packets are initialized at time $t = 0$ in the region $y < 0$ and travel in opposite directions. Consequently, the left-moving wave packet eventually crosses the boundary, re-enters from the opposite side, and travels towards the 2D material located at $y = 0$. At sufficiently long times, this wave packet will either overlap with the right-propagating packet or interact with the 2D material. In the results presented in this work, such artifacts arising from the application of PBCs have been carefully avoided by limiting the simulation time. Thus, when we refer to “asymptotic” expectation values for long times (e.g. $t \rightarrow +\infty$, as in the case of Sect. III A), we mean that these times are long enough for the interaction between the right-moving wave packet and the 2D material to be complete, yet short enough to eliminate artifacts due to PBCs.

A. Photon dynamics

We start by looking at the transmission of the photon beam across the 2D material. We compute the spatio-

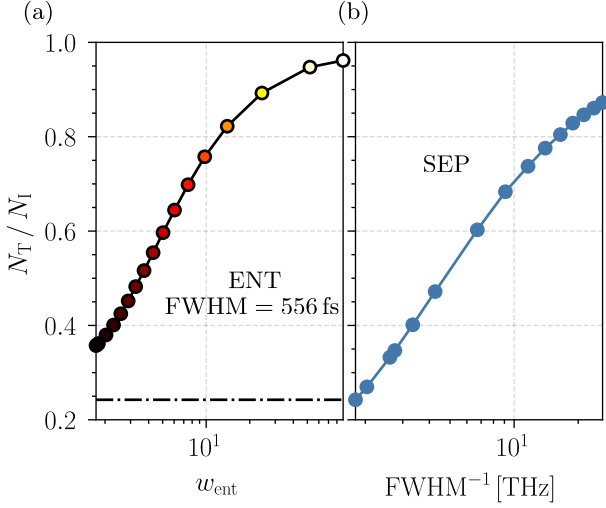


FIG. 4. Panel (a) Number of transmitted photons for entangled packets at a fixed FWHM ≈ 556 fs, as a function of the entanglement parameter w_{ent} —see Eq. (5). The color scale on the dots indicates the value of the entanglement entropy, from minimum (dark) to maximum (bright). The horizontal dash-dotted line indicates the number of transmitted photons for a separable packet of the same FWHM. Panel (b) Number of transmitted photons for separable packets as a function of the inverse of the FWHM. The separable packet with the largest width in panel (b) has the same FWHM as the entangled packets in panel (a).

temporal evolution of the linear density of photons

$$n_{\text{pht}}(t, y) = \frac{1}{L_y} \sum_{kk'} e^{-i(k-k')y} \langle \hat{a}_k^\dagger \hat{a}_{k'} \rangle(t), \quad (7)$$

where $\langle \hat{a}_k^\dagger \hat{a}_{k'} \rangle(t) \equiv \langle \Phi | \hat{a}_k^\dagger(t) \hat{a}_{k'}(t) | \Phi \rangle$ with $\hat{a}_k^\dagger(t) = e^{i\hat{H}t} \hat{a}_k^\dagger e^{-i\hat{H}t}$ and $\hat{a}_{k'}(t) = e^{i\hat{H}t} \hat{a}_{k'} e^{-i\hat{H}t}$. Spatial integration of the linear density gives the total number of photons

$$N_{\text{pht}}(t) = \int_{-\frac{L_y}{2}}^{\frac{L_y}{2}} dy n_{\text{pht}}(t, y) = \sum_k \langle \hat{a}_k^\dagger \hat{a}_k \rangle(t). \quad (8)$$

It is important to note that, because of the light-matter interaction, the total number of photons is not conserved during the dynamics, and it reduces to its initial value in the asymptotic limit $N_{\text{pht}}(t \rightarrow \infty) = N_{\text{pht}}(0)$.

In Fig. 3, we show two examples of the spatio-temporal evolution of the left- and right-propagating entangled packets for $w_{\text{ent}} = 1.73$. Fig. 3(a) shows the free propagation of the packets in the absence of the material, whereas Fig. 3(b) shows the interaction of the right-propagating packet with the material placed at $y = 0$. Due to the interaction with the material, the photon wave packet gets partially transmitted and partially reflected. We define the total transmission by computing the fraction of photons found on the right of the 2D material, in the

asymptotic limit

$$N_T = \int_0^{\frac{L_y}{2}} dy n_{\text{pht}}(t \rightarrow \infty, y). \quad (9)$$

In Fig. 4(a), we show the total transmission for a series of entangled pulses with increasing entanglement parameter w_{ent} , at a fixed FWHM. For increasing entanglement parameter w_{ent} , we observe an overall enhancement of the total photon transmission. This can be understood as a direct consequence of the fact that, due to the broader distribution of frequencies centered around the ω_0 resonance, see Fig. 2(a), strongly entangled packets contain an increasing number of off-resonant components. In Fig. 4(b), we report the transmission for separable packets as a function of the inverse of their FWHM. Overall, we observe a striking similarity between the transmission of entangled packets of increasing entanglement parameter w_{ent} and fixed FWHM, and the transmission for separable packets of decreasing FWHM. In the separable case, the transmission increases by reducing the packet width. By considering the separable packet of the same width of the entangled ones, we see that its transmission is smaller than the one for an entangled packet. In particular, in the limit of weakly entangled packets, the transmission seems to show a convergent behavior towards the transmission of a separable packet of the same FWHM, even though convergence is never reached within the range of parameters we have considered.

In Fig. 5 we show the temporal evolution of the density of transmitted photons computed at a point $y_f > 0$ at large distance from the material, i.e. $n_T(t) \equiv n_{\text{pht}}(t, y = y_f)$ —see the vertical dashed line in Fig. 3(b). We compare the transmitted density with the incident one $n_I(t)$, which is defined as the photon density associated with a packet that propagates freely without interacting with the material, corresponding to a vertical cut in Fig. 3(a). For visualization purposes, we change time variable from t to $\tau \equiv t - t_f$, where t_f represents the arrival time of the peak of the freely propagating packet at the position y_f —see Fig. 3(a). For weakly entangled ($w_{\text{ent}} = 1.73$) and separable packets, see Fig. 5(a) and (d), respectively, the transmitted packets show a double-peak structure indicating a temporal delay between the photon density that is transmitted without being absorbed by the material (peak at negative τ) and the photons that are absorbed and re-emitted (peak at positive τ). Notably, as the entanglement parameter w_{ent} increases, the double peak structure progressively disappears, see Fig. 5(b) and (c). From the latter panel (corresponding to $w_{\text{ent}} = 88.36$) we clearly see that, for strongly entangled photons, the transmitted packet becomes almost synchronous to the incident one. In Fig. 5(e), we show the crossover between the delayed and synchronized transmission regimes by plotting the temporal position of the two peaks in the transmitted packet as a function of w_{ent} . We see that for $w_{\text{ent}} \approx 7$ the two peaks disappear, merging onto a single one.

The reader may be tempted to interpret the existence

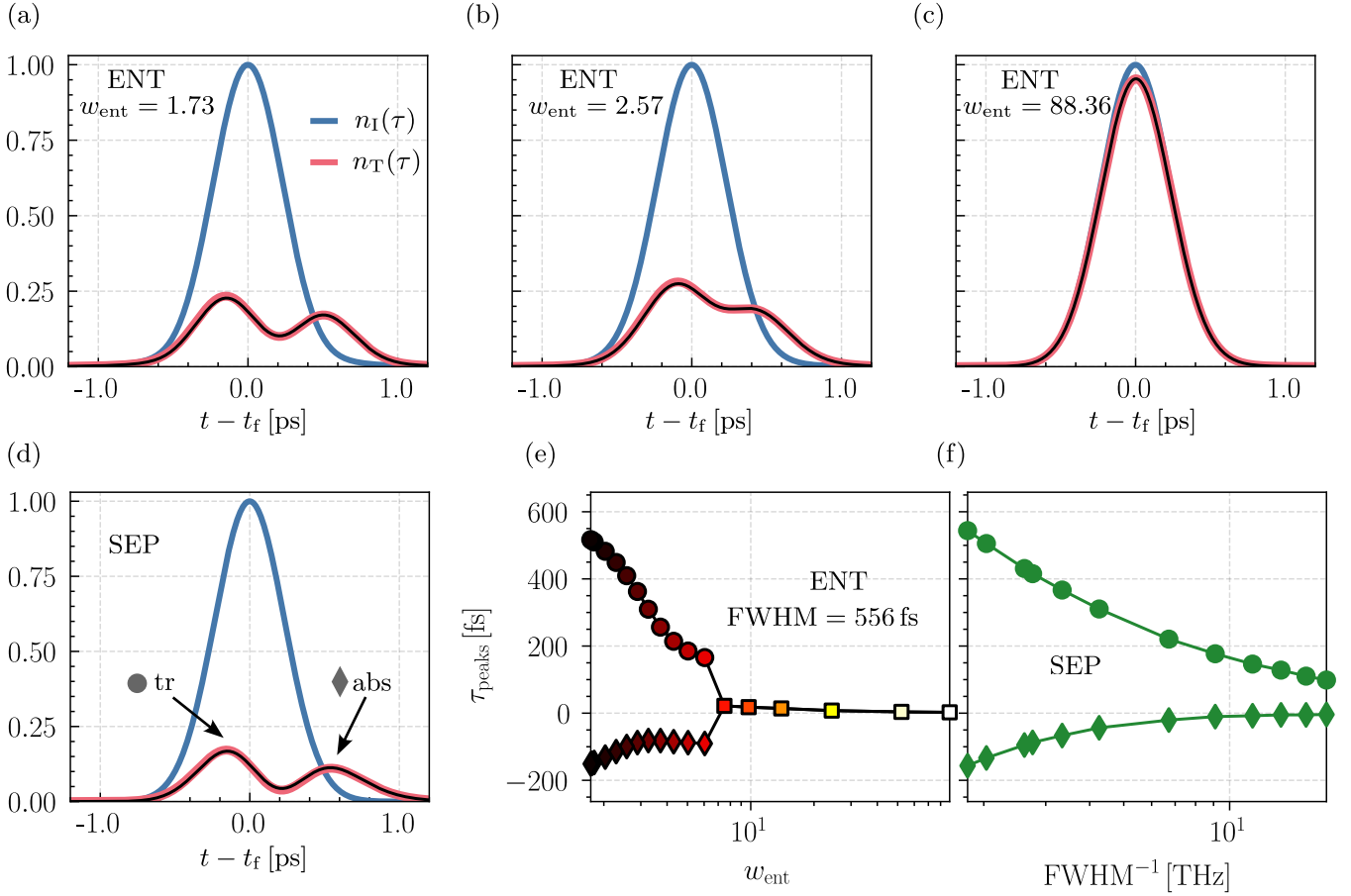


FIG. 5. Panels (a)-(d) Temporal evolution of the density of transmitted photons (orange line) as a function of the delay time $\tau = t - t_f$, where t_f is the arrival time of the peak of the freely propagating photon wave packet (blue lines) at the same position $y_f \gg 0$. The incident wave packets have a FWHM of approximately 556 fs in all panels from (a) to (d). All the photon densities are normalized to the peak value of the corresponding incident density. In panels (a)-(c) we display the temporal evolution of entangled packets. In particular, results in panel (a) have been obtained by setting $w_{\text{ent}} \approx 1.73$ and $\tau_{\text{ent}} \approx 101.88$ fs. Results in panel (b) correspond to: $w_{\text{ent}} \approx 2.57$ and $\tau_{\text{ent}} \approx 79.17$ fs. Finally, results in panel (c) correspond to $w_{\text{ent}} \approx 88.36$ and $\tau_{\text{ent}} \approx 2.63$ fs. Panel (d) refers to a separable packet with $\tau_{\text{sep}} \approx 232.71$ fs. The entanglement parameter w_{ent} and the time scales τ_{ent} and τ_{sep} are defined in Eqs. (4)-(6). The thin black lines represent the transmitted densities evaluated by using Eq. (11). The circle and diamond symbols in panel (d) highlight the transmission (tr) and absorption (abs) peaks of the transmitted packet. Panel (e) Transmission (circles) and absorption (diamonds) peaks for entangled packets with FWHM ≈ 556 fs as functions of the entanglement parameter w_{ent} . The squares indicate the single peak of the transmitted packet when the distinction between transmission and absorption peaks is lost. The color scale on the symbols of panel (e) indicates the value of the entanglement entropy characterizing the incident packet, from minimum (dark) to maximum (bright). Panel (f) Transmission (circles) and absorption (diamonds) peaks for separable packets as functions of the inverse FWHM.

of a single peak at large w_{ent} —see Fig. 5(c)—as the result of the decrease in height of the absorption peak, i.e. the peak occurring for positive values of τ in Figs. 5(a), (b), and (d), in favor of the transmission peak. In order to test this hypothesis, we analyze in Fig. 5(f) the dependence of the transmission and absorption peaks on the FWHM, for the case of separable packets. This analysis is pertinent since, as we have seen in Fig. 4(a), by decreasing the FWHM, the total transmission of separable packets increases and approaches the transmission of the entangled packets with large w_{ent} . As clearly seen in Fig. 4(f), separable packets *always* display two peaks, even in the case of very small values of the FWHM on the

order of ≈ 53 fs for which the transmission of entangled and separable packets become equivalent. We conclude that the absence of the two-peak structure for large w_{ent} is a genuine consequence of entanglement and not merely due to the increase of transmission.

To gain further insight, we investigate the inner structure of the density profiles of the transmitted photons. From Eq. (7), we see that the linear photon density is completely determined by the distribution of photon occupation numbers, $\langle \hat{a}_k^\dagger \hat{a}_{k'} \rangle(t)$, which, at a fixed time t , depends on the two frequencies $(\omega_k, \omega_{k'})$. It is important to stress that nearly identical photon density profiles may

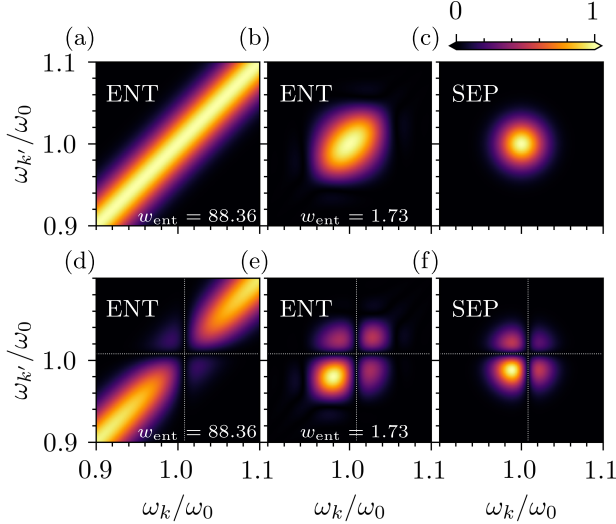


FIG. 6. Modulus of the photon number distribution, $|\langle \hat{a}_k^\dagger \hat{a}_{k'} \rangle|$ for $k, k' \geq 0$, of the incident (a)-(c) and transmitted (d)-(f) packets, normalized to their maximum value. Results in panels (a) and (d) refer to the entangled case with $\tau_w \approx 232.02$ fs and $\tau_{\text{ent}} \approx 2.63$ fs, corresponding to $w_{\text{ent}} \approx 88.36$. Results in panels (b) and (e) refer to the entangled case with $\tau_w \approx 176.59$ fs and $\tau_{\text{ent}} \approx 101.88$ fs, corresponding to $w_{\text{ent}} \approx 1.73$. Finally, results in panels (c) and (d) refer to the separable case with $\tau_{\text{sep}} \approx 232.71$ fs. The entanglement parameter w_{ent} and the time scales τ_{ent} and τ_{sep} are defined in Eqs. (4)-(6).

correspond to very different distributions of photon occupation numbers $\langle \hat{a}_k^\dagger \hat{a}_{k'} \rangle$. For example, this is readily seen in panels (a)-(c) of Fig. 6, where we present plots of $\langle \hat{a}_k^\dagger \hat{a}_{k'} \rangle_0 \equiv \langle \hat{a}_k^\dagger \hat{a}_{k'} \rangle(t=0)$ for $w_{\text{ent}} = 88.36$ (strong entanglement), $w_{\text{ent}} = 1.73$ (weak entanglement), and separable incident packets, respectively. These three situations correspond to the plots in panels (c), (a), and (d) of Fig. 5, where we clearly see that the initial photon density profiles (blue curves) are practically identical.

In panels (d)-(f) of Fig. 6, we show the same occupation numbers $\langle \hat{a}_k^\dagger \hat{a}_{k'} \rangle(t=t_f)$ but computed at the instant of time t_f , that is after the interaction of the wave packets with the 2D material. The frequency distributions remain identical to the incident ones except for a sharp suppression of $\langle \hat{a}_k^\dagger \hat{a}_{k'} \rangle$ along the axes $\omega_k = \omega_*$ and $\omega_{k'} = \omega_*$, which signal the resonant absorption of the components of the initial packets at frequency ω_* . From this observation, we define the transmission coefficients T_k by expressing the distribution of photon numbers $\langle \hat{a}_k^\dagger \hat{a}_{k'} \rangle(t)$ at time t in terms of the distribution $\langle \hat{a}_k^\dagger \hat{a}_{k'} \rangle_0$ of the incoming photons. Specifically, we *impose*

$$\langle \hat{a}_k^\dagger \hat{a}_{k'} \rangle(t) \stackrel{!}{=} \langle \hat{a}_k^\dagger \hat{a}_{k'} \rangle_0 |T_k^* T_{k'}| e^{i(k-k')(y_i + ct)}, \quad (10)$$

where the phase factor takes into account the translation of the packet from the initial position y_i , see Fig. 1.

We extract the transmission coefficients T_k from Eq. (10) by using a single broadband separable initial

packet and write, for all types of different incident packets (i.e. separable and entangled), the following expression for the transmitted photon density $n_T(\tau)$:

$$n_T(\tau) = \frac{1}{L_y} \sum_{\{k, k'\} > 0} e^{i(\omega_k - \omega_{k'})\tau} |\langle \hat{a}_k^\dagger \hat{a}_{k'} \rangle_0| T_k^* T_{k'}. \quad (11)$$

We follow this procedure to produce the thick black lines in panels (a)-(d) of Fig. 5. We conclude that Eq. (11) reproduces extremely well the density profiles computed from the exact unitary dynamics. The transmission coefficients T_k are well described by the following packet-independent expression

$$T_k = \frac{\omega_k - \omega_*}{\omega_k - \omega_* + i\Gamma/2}, \quad (12)$$

where Γ is the spontaneous decay rate of the matter degrees of freedom, which we calculate from perturbation theory, i.e. $\Gamma \approx 6.97$ THz—see Appendix C.

These observations show that all the information about the transmitted density $n_T(\tau)$ is contained in the distribution $\langle \hat{a}_k^\dagger \hat{a}_{k'} \rangle_0$ of the photon occupation numbers of the incident packets. We therefore propose a simple analytical model in which $\langle \hat{a}_k^\dagger \hat{a}_{k'} \rangle_0$ is parametrized by an elliptical distribution in the $(\omega_k, \omega_{k'})$ plane, centered around the resonance frequency ω_0 :

$$|\langle \hat{a}_k^\dagger \hat{a}_{k'} \rangle_0| \approx N^2 e^{-[(\omega_k - \omega_0)^2 + (\omega_{k'} - \omega_0)^2] \frac{\tau_1^2 + \tau_2^2}{4}} \times e^{(\omega_k - \omega_0)(\omega_{k'} - \omega_0) \frac{\tau_1^2 - \tau_2^2}{2}}. \quad (13)$$

Here, τ_1 and τ_2 represent the effective major and minor semi-axes of the elliptical distribution and N is a normalization constant. For $\tau_1 = \tau_2$, the distribution is that of a separable packet, namely $|\langle \hat{a}_k^\dagger \hat{a}_{k'} \rangle_0|^2 = n_k n_{k'}$, where n_k is the photon occupation number at wave-number k . The Gaussian shape leads to a spherical-symmetric distribution, reproducing extremely well the photon number distribution of the separable case shown in panel (c) of Fig. 6. On the contrary, entangled packets are described by the choice $\tau_2 < \tau_1$, which shrinks and enlarges the frequency distribution along the $\omega_{k'} = 2\omega_0 - \omega_k$ and $\omega_{k'} = \omega_k$ axes, respectively, see panels (a)-(b) of Fig. 6.

Thanks to this parametrization, we can transform the momentum sum in Eq. (11) into a frequency integral. Implementing the change $\omega - \omega_0 \rightarrow \omega$, $\omega' - \omega_0 \rightarrow \omega'$ of integration variables, we can rewrite the transmitted photon density as

$$n_T(\tau) = N^2 \iint_{-\infty}^{+\infty} d\omega d\omega' e^{i(\omega - \omega')\tau} \times e^{-\omega^2 \tau_+^2/2} e^{-\omega'^2 \tau_+^2/2} e^{\omega \omega' \tau_-^2} T^*(\omega) T(\omega'), \quad (14)$$

where we have introduced $2\tau_\pm^2 \equiv \tau_1^2 \pm \tau_2^2$. Notice that τ_- is always a real variable as $\tau_2 < \tau_1$.

Separable packets can be obtained from Eq. (14) by taking the $\tau_- \rightarrow 0$ limit. In this limit, the integrand in Eq. (14) factorizes and the transmitted photon density

can be simply written as the square modulus of a single wavefunction $\Psi_0(\tau)$:

$$\lim_{\tau_- \rightarrow 0} n_T(\tau) = \Psi_0^*(\tau) \Psi_0(\tau). \quad (15)$$

$\Psi_0(\tau)$ can be expanded in frequency domain as

$$\Psi_0(\tau) = \int_{-\infty}^{+\infty} d\omega e^{-i\omega\tau} \psi(\omega), \quad (16)$$

where

$$\psi(\omega) = N e^{-\omega^2 \tau_+^2/2} T(\omega) \quad (17)$$

and N is a normalization constant.

For entangled packets, i.e. for a generic value of τ_- , we expand the exponential factor $e^{\omega\omega'\tau_-^2}$ in Eq. (14) in powers of τ_- around $\tau_- = 0$, and write the transmitted photon density as an infinite sum of densities associated to elementary wavefunctions $\Psi_j(\tau)$:

$$n_T(\tau) = \sum_{j=0}^{\infty} \Psi_j^*(\tau) \Psi_j(\tau), \quad (18)$$

where $\Psi_j(\tau)$ is defined by the j -th moment of spectral function $\psi(\omega)$ introduced in Eq. (16). Specifically, we have

$$\Psi_j(\tau) = \frac{\tau_-^j}{\sqrt{j!}} \langle \omega^j \rangle(\tau), \quad (19)$$

with

$$\langle \omega^j \rangle(\tau) \equiv \int_{-\infty}^{+\infty} d\omega \omega^j e^{-i\omega\tau} \psi(\omega). \quad (20)$$

Further technical details are reported in Appendix E.

Eqs. (18)-(20) show that the transmitted photon density $n_T(\tau)$ for entangled packets can be represented as an infinite superposition of *separable* packets, each characterized by an elementary density $n_j(\tau)$ determined by a single wavefunction $\Psi_j(\tau)$, i.e. namely

$$n_T(\tau) = \sum_{j=0}^{\infty} n_j(\tau), \quad (21)$$

with

$$n_j(\tau) \equiv \Psi_j^*(\tau) \Psi_j(\tau). \quad (22)$$

As we have seen above, the transmitted photon density in the case of separable packets is represented by a single elementary contribution, see Eq. (15). In contrast, entangled packets, corresponding to $\tau_- > 0$, are represented by a superposition of non-entangled packets $n_j(\tau)$, as in Eqs. (21)-(22), with a spread controlled by the parameter τ_- , see Eq. (19). The larger the entanglement parameter, the larger is the number of elementary contributions $n_j(\tau)$ that needs to be taken into account to have a faithful representation of the transmitted density.

To further investigate the structure of the elementary contributions, we first analyze $n_j(\tau)$ by assuming that no interaction occurs between the incident photons and the 2D material. This is achieved by setting $\Gamma \rightarrow 0$ in the definition (12) of the transmission coefficient T_k . In this limit, $T(\omega) \rightarrow 1$ for all frequencies, and the moments $\langle \omega^j \rangle$ in Eq. (20) can be computed analytically. Indeed, the quantity $\psi(\omega)$ in Eq. (17) reduces to $\psi^{(0)}(\omega) = N e^{-\omega^2 \tau_+^2/2}$ and the corresponding elementary photon densities can be expressed in closed form as

$$n_j^{(0)}(\tau) = \frac{N^2}{j!} \left(\frac{\tau_-^2}{2\tau_+^2} \right)^j e^{-\tau^2/\tau_+^2} H_j^2 \left(\frac{\tau}{\sqrt{2}\tau_+} \right), \quad (23)$$

where the superscript (0) indicates that Eq. (23) refers to freely propagating photons and $H_j(x) = (-1)^j e^{x^2} d^j[e^{-x^2}]/dx^j$ are the Hermite polynomials. Since Eq. (23) displays the product between a Gaussian and the Hermite polynomial $H_j(x)$, and since the latter has j zeros, the photon density $n_j^{(0)}(\tau)$ —associated with each of the separable contributions to the entangled pulse—represents a train of $j+1$ pulses whose width decreases with increasing order j . We explicitly show this in Fig. 7 (blue lines) where we plot $n_j^{(0)}(\tau)$ for different values of j .

We now analyze the case of photons interacting with the material by computing the moments $\langle \omega^j \rangle$ in Eq. (20) corresponding to a transmission coefficient $T(\omega) \neq 1$. For the sake of analytical amenability, we compute the moments $\langle \omega^j \rangle$ for $T(\omega) \neq 1$ by taking $\omega_* = \omega_0$ in Eq. (12) and carrying out the quadrature in Eq. (16) analytically, see Appendix E. The result of this calculation for different values of j and specific values of τ_+ and τ_- is shown in Fig. 7 (red curves). As seen by comparing incident (blue curves) and transmitted (red curves) photon densities, the largest [smallest] contribution to the absorption [transmission] comes from small values of j . For these values of j , the interaction of photons with the collective mode of the 2D material clearly splits the separable packets $n_j(\tau)$ into transmitted and absorbed contributions, giving rise to an additional peak in the density (with respect to the incident density): see red curves in panels (a)-(b) of Fig. 7 corresponding to $j=0$ and $j=1$, respectively.

For $\tau_- = 0$ (corresponding to the case in which incident photons are in a separable state), only the $j=0$ elementary contribution is different from zero. Our simple analytical model therefore consistently captures the double peak structure of the transmitted density seen in Fig. 5(d). On the contrary, the case of incident entangled photons is described in our analytical model in terms of a large superposition of higher-order elementary contributions with $j > 0$. In particular, for strongly entangled packets, the interaction with the collective mode involves the absorption of several elementary contributions with j up to ~ 10 —see panels (c)-(d) in Fig. 7. To better appreciate this point, we plot in Fig. 8 the total number of photons N_j carried by each $n_j(\tau)$. Specifically, we

introduce two quantities:

$$N_j^{(0)} \equiv c \int_{-\infty}^{+\infty} d\tau n_j^{(0)}(\tau) \quad (24)$$

and

$$N_{T,j} \equiv c \int_{-\infty}^{+\infty} d\tau n_j(\tau). \quad (25)$$

For weakly entangled packets, the number of photons carried by each contribution exponentially decays with the order j . As the entanglement parameter increases, the distribution evolves towards a power-law decay, showing the increasing importance of elementary contributions with large j , i.e. the importance of taking into account multiple separable trains with an increasing number of shorter and shorter pulses. In summary, for strongly entangled packets, as a result of the importance of the $j > 0$ contributions in the expansion (18), the interaction process between matter and time-energy entangled photons effectively includes absorption and re-emission processes taking place on time scales much shorter than the temporal width of the incident packet.

We can use these results to rationalize the origin of the synchronization phenomenon observed in Fig. 5. For large values of w_{ent} , Fig. 5(c), the role of elementary contributions $n_j(\tau)$ with large $j > 0$ is dominant. Since these are transmitted with no delay—as seen in Fig. 7(c) and (d)—the entangled packet in Fig. 5(c) gets transmitted as a whole with negligible delay between transmission and absorption peaks.

B. Ultrafast light-induced matter excitation

We now focus on the consequences of the entangled photon driving on the dynamics of the light-stimulated matter excitations. We investigate the energy stored in the matter degrees of freedom:

$$E_{\text{mat}}(t) = \hbar\omega_0 \langle \Phi | \hat{b}^\dagger(t) \hat{b}(t) | \Phi \rangle \equiv \hbar\omega_0 \langle \hat{b}^\dagger \hat{b} \rangle(t). \quad (26)$$

This quantity measures the number of collective excitations induced by light in the material. Experimental characterizations of this quantity usually rely on pump-probe setups in which the light-stimulated material is probed after a time delay. Relevant observables depend on the microscopic details of the excitation described by the stimulated collective mode. Specific examples include effective non-equilibrium temperatures determined via transient reflectivity in the case of collective excitations of electronic origin [81–84] and transient lattice displacements in the case of light-stimulation of phonons [85, 86].

In Fig. 9(a)-(b), we illustrate the dynamics of the matter energy for entangled and separable incident packets of the same temporal width. Here, we measure time with respect to the reference time $t_i \equiv |y_i|/c$ which corresponds to the arrival time of the peak of the incident photon packet at the position of the 2D material (i.e. $y = 0$). As

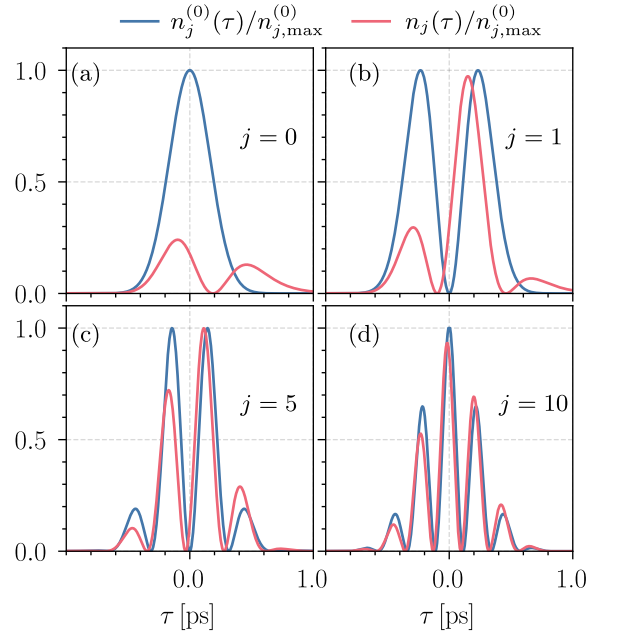


FIG. 7. The elementary contribution $n_j(\tau)$ —defined in Eq. (22)—plotted as a function of the delay time $\tau = t - t_f$ for different values of j . Here, t_f is the arrival time of the peak of the incident wave packet. Each curve is normalized to the maximum value $n_{j,\text{max}}^{(0)}$ of the incident packet. Blue lines represent the incident wave packet—defined in Eq. (23)—while red lines represent the transmitted packet. Data in this figure have been obtained by setting $\tau_+ \approx 232.76$ fs and $\tau_- \approx 232.67$ fs, corresponding to $\tau_1 \approx 329.11$ fs and $\tau_2 \approx 6.58$ fs in Eq. (13).

a function of time, the energy shows a bell-like shape indicating power absorption $\partial_t E_{\text{mat}} > 0$ followed by power emission $\partial_t E_{\text{mat}} < 0$. As a direct consequence of the enhanced transmission discussed in Figs. 4–5, the amount of electromagnetic energy absorbed by the 2D material in the entangled case, as measured by the peak value $E_{\text{mat,max}}$ of E_{mat} , is much smaller with respect to the energy absorbed in the case of a separable packet of the same FWHM. In panels (c)-(d) of Fig. 9, we report the peak energies $E_{\text{mat,max}}$ for various entangled and separable incident packets. In the entangled case, Fig. 9(c), we plot $E_{\text{mat,max}}$ as a function of the entanglement parameter w_{ent} , at a fixed FWHM. In the separable case instead, Fig. 9(d), we plot $E_{\text{mat,max}}$ as a function of the inverse of the FWHM. These two plots emulate, in spirit, Fig. 4.

We start by describing $E_{\text{mat,max}}$ for separable packets, Fig. 9(d). For ultrashort separable packets, i.e. large values of FWHM^{-1} , $E_{\text{mat,max}}$ is an increasing function of the pulse width (decreasing function of FWHM^{-1}). $E_{\text{mat,max}}$ reaches a maximum for FMHW ≈ 191.89 fs of the order of the inverse decay rate $\sim \Gamma^{-1}$. This is due to the fact that, for larger FWHM, the bandwidth of the incoming photons starts to display a smaller overlap with the absorption bandwidth of the medium. The increase of $E_{\text{mat,max}}$ with increasing FWHM for short pulses is a direct consequence of the decrease in the number of

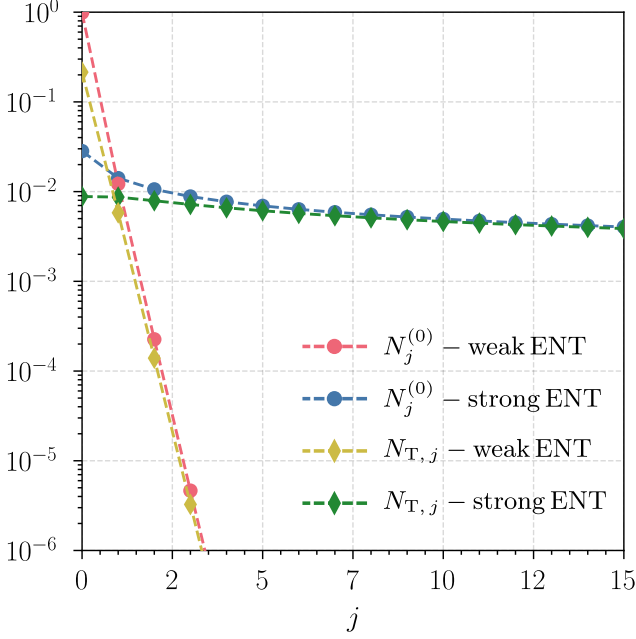


FIG. 8. Total number of photons carried by the j -th elementary contribution n_j for the incident wave packets ($N_j^{(0)}$, filled circles) and the transmitted wave packets ($N_{T,j}$, diamonds) in the analytical model. The quantities $N_j^{(0)}$ and $N_{T,j}$ have been defined in Eqs. (24) and (25), respectively. Results for the strongly entangled [weakly entangled] case have been evaluated by setting $\tau_+ \approx 232.76$ fs and $\tau_- \approx 232.67$ fs [$\tau_+ \approx 325.12$ fs and $\tau_- \approx 51.08$ fs].

transmitted photons discussed in Fig. 4(b). On the other hand, the decrease of $E_{\text{mat,max}}$ for larger values of the FWHM pulses indicates the approach towards an “adiabatic regime” in which the peak of the energy absorbed by the 2D material follows the peak of the energy of the incoming pulse. Moving to the case of entangled packets of fixed FWHM, Fig. 9(c), we observe that the peak energy monotonously decreases by increasing the entanglement parameter w_{ent} . In the limit of weak entanglement, $E_{\text{mat,max}}$ converges towards the value obtained for a separable packet of the same FWHM.

Besides the above quantitative aspects, we now show how entanglement in the incoming photon packet qualitatively changes the dynamics of the matter degrees of freedom by suppressing the delay between the arrival of the perturbation and the creation of the excitation. In Fig. 10(a), we show plots of $E_{\text{mat}}(t)$ as a function of time, normalized to the corresponding peak values. In both entangled and separable cases, the peak energy is reached for an instant of time $t_{\text{peak}} > t_i$ simply indicating that, due to causality, energy absorption is delayed with respect to the arrival of the perturbation. However, we clearly see that the peak in the case of the entangled packets occurs before the one in the case of separable packets indicating that, in the entangled case, energy is absorbed by matter at a faster pace.

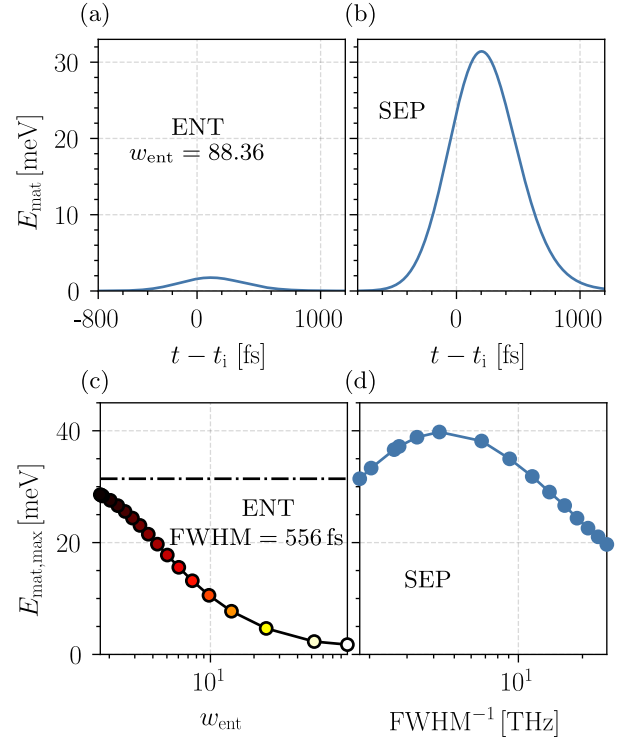


FIG. 9. (a)-(b) Energy of the matter degrees of freedom, Eq. (26), as a function of time measured with respect to the arrival time t_i of the peak of the incident packet. Panel (a) refers to an entangled packet with $\tau_{\text{ent}} \approx 2.63$ fs and $\tau_w \approx 232.02$ fs, corresponding to an entanglement parameter $w_{\text{ent}} \approx 88.36$. Panel (b) refers to a separable packet for $\tau_{\text{sep}} \approx 232.71$ fs. Panel (c) The peak energy induced by entangled packets is plotted as a function of the entanglement parameter w_{ent} . As usual, the color scale on the symbols in panel (c) indicates the value of the entanglement entropy characterizing the incident packet, from minimum (dark) to maximum (bright). The FWHM of the entangled wave packets in panel (c) has a fixed value of approximately 556 fs. Panel (d) The peak energy induced by separable packets is plotted as a function of the inverse of the FWHM. The horizontal dash-dotted line indicates the peak energy for a separable packet of the same FWHM of the entangled packets.

In order to confirm that this feature (i.e. the fact that energy is absorbed at a faster pace in the entangled case) is a genuine consequence of entanglement, we check how the delay between the separable and entangled cases depends on (i) the width of the packets and (ii) the overall absorbed energy. In Fig. 10(b), we show that such delay persists in the case of separable and entangled packets of reduced FWHM. We notice that, in this case, the temporal profiles $E_{\text{mat}}(t)$ acquire an asymmetric shape due to the fact that the FWHM of the considered initial photon packets is smaller than the spontaneous decay time of the matter degrees of freedom. We now proceed to rule out the possibility that the delay is due to the fact that, for incident packets that have the same width, much less energy is absorbed in the entangled case with respect to the

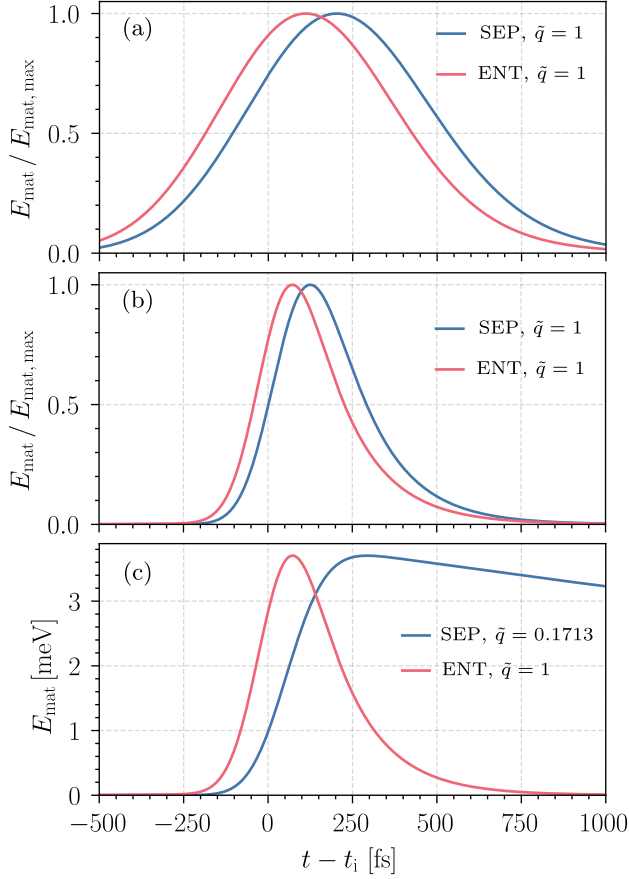


FIG. 10. The energy of the matter degrees of freedom, $E_{\text{mat}}(t)$, as defined in Eq. (26), is plotted as a function of time measured with respect to the arrival time t_i of the peak of the incident wave packet. Panel (a) Energy normalized by its peak value induced by an entangled wave packet (orange line) with $\tau_{\text{ent}} \approx 2.63$ fs and $\tau_w \approx 232.02$ fs, see Eq. (4), corresponding to $w_{\text{ent}} \approx 88.36$, Eq. (5), and a separable packet (blue line) with $\tau_{\text{sep}} \approx 232.71$ fs, see Eq. (6). (b) Energy normalized by its peak value, induced by an entangled wave packet (orange line) with $\tau_{\text{ent}} \approx 2.63$ fs and $\tau_w \approx 77.57$ fs corresponding to $w_{\text{ent}} \approx 29.54$, and a separable packet (blue line) with $\tau_{\text{sep}} \approx 77.57$ fs. (a)-(b) are both evaluated considering an effective charge $\tilde{q} = 1$. (c) Energy induced by an entangled wave packet (orange line), evaluated with an effective charge $\tilde{q} = 1$, having $\tau_{\text{ent}} \approx 2.63$ fs, $\tau_w \approx 77.57$ fs and $w_{\text{ent}} \approx 29.54$, and a separable packet (blue line) with $\tau_{\text{sep}} \approx 77.57$ fs evaluated with an effective charge $\tilde{q} = 0.1713$ such that it matches the matter energy peak value induced by the entangled wave packet.

separable one — as observed in Fig. 9(a)-(b). To this end, in Fig. 10(c), we compare the temporal profiles $E_{\text{mat}}(t)$ in the case of entangled and separable initial packets of equal widths, and giving rise to the same peak energies in the matter degrees of freedom. Specifically, we take two incident packets of the same FWHM and, for the separable case, we reduce the light-matter coupling constant by reducing the effective charge \tilde{q} to make sure that the peak energy in the separable case matches the one reached in

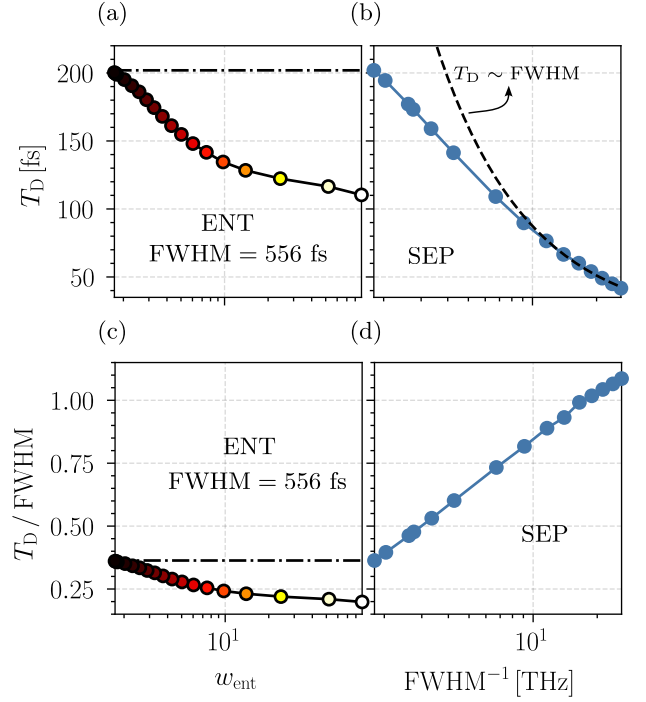


FIG. 11. Panel (a) The excitation delay time T_D , defined in the main text as $T_D \equiv t_{\text{peak}} - t_i > 0$, is plotted as a function of the entanglement parameter w_{ent} for incident entangled wave packets. Panel (b) The delay time T_D is plotted as a function of the inverse of the FWHM for incident separable packets. The dashed black line in panel (b) represents the linear trend obtained by fitting the data for the six shortest pulses with the linear model $T_D = \text{coefficient} \times \text{FWHM} + \text{const.}$ Panels (c)-(d) show the ratio T_D/FWHM . The color scale on the symbols of panels (a) and (c) indicates the entanglement entropy, from minimum (dark) to maximum (bright). The horizontal dash-dotted lines in panels (a) and (c) indicate T_D and T_D/FWHM for separable packets of the same FWHM of the entangled packets.

the entangled case for $\tilde{q} = 1$. The reduced coupling constant in the separable case ($\tilde{q} = 0.1713$) suppresses the spontaneous decay rate, giving rise to a much more pronounced asymmetry between creation and decay of the excitation. Nonetheless, as we clearly see in Fig. 10(c), t_{peak} in the case of a separable packet (blue curve) occurs *after* the one in the entangled case (red curve).

We now introduce the excitation delay time, T_D , defined as the difference the time at which the matter energy $E_{\text{mat}}(t)$ reaches its maximum value and the time at which the peak in the incident photon density reaches the 2D material, i.e. $T_D \equiv t_{\text{peak}} - t_i > 0$. Fig. 11 shows the excitation delay time T_D for separable and entangled incident packets, at $\tilde{q} = 1$. For separable packets, panel (b), we plot T_D as a function of the inverse of the FWHM, whereas, in panel (a), we plot T_D for entangled packets of a fixed FWHM, as a function of the entanglement parameter w_{ent} . For ultrashort separable packets—Fig. 11(b)—the excitation delay time increases linearly

with the FMHW. For wider pulses (smaller FMHW^{-1}), the linear trend turns into a sublinear growth. This can be readily appreciated by looking at the dashed line in Fig. 11(b) obtained by fitting the data corresponding to the six shortest pulses (i.e. the six rightmost scattered points in the figure) with a linear model $T_D = \text{coefficient} \times \text{FWHM} + \text{const.}$ For entangled packets at fixed FWHM—Fig. 11(b)—the excitation delay converges, for small values of the entanglement parameter, w_{ent} to the value obtained for a separable packet of the same FWHM. Remarkably, by increasing w_{ent} , T_D quickly decreases becoming significantly smaller than the FWHM (556 fs).

Comparing Fig. 11(a) with Fig. 11(b), together with the analogous observations in the case of $E_{\text{mat,max}}$ in Fig. 9(c)-(d), we see that, as the entanglement parameter increases (for a fixed value of the FWHM), it is as if the matter degrees of freedom are being stimulated by separable packets of progressively smaller and smaller width.

We notice that the decrease of the excitation delay T_D for entangled packets of increasing entanglement parameter w_{ent} has a sharply different origin, as compared to the separable case. By considering the definition of the entanglement parameter w_{ent} , Eq. (5), we observe that the increase of w_{ent} is controlled by the decrease of τ_{ent} which is an intrinsic time scale of the entangled pair previously introduced in Eq. (4). Specifically, upon reducing τ_{ent} the range over which the frequencies of the two partners of the entangled pair are anti-correlated increases. This shows that, in the entangled case, the decrease of T_D is intimately related to the strong frequency correlation between the packet interacting with the material and the packet freely propagating in the opposite direction depicted in Fig. 1. In contrast, the decrease of T_D in the separable case is trivially controlled by the shorter duration of the pulse.

To further highlight this difference, we plot in panels (c)-(d) of Fig. 11 the excitation delay T_D normalized to the FWHM of the incoming packet. For separable pulses—panel (d)— T_D/FWHM increases by decreasing the FWHM. On the contrary, for entangled packets—panel (c)— T_D/FWHM decreases as a function of the entanglement parameter. We conclude that entangled photons offer a key advantage with respect to separable packets. In the former case, working with packets of a fixed FWHM, one can induce an ultrafast dynamics of the matter degrees of freedom by increasing w_{ent} , i.e. reducing the inner time scale τ_{ent} .

Once again, we can rationalize the above observations by invoking the expansion (18) of an entangled packet in terms of an infinite superposition of trains of short separable pulses. The decrease of the excitation delay T_D with increasing w_{ent} is a clear signature of the fact that, as shown in Fig. 8, strongly entangled packets contain trains of ultrafast separable pulses which are mathematically represented by the elementary contributions with $j \gg 1$ in Eq. (18). As a result, stimulating matter degrees

of freedom with entangled packets is similar to stimulating them with ultrafast separable packets. At the same time, due to the fact that a large contribution of the absorbed energy comes from the $j = 0$ elementary contribution, the delay T_D in the limit $w_{\text{ent}} \gg 1$ remains always larger as compared to the ultrashort separable packets, as seen in Fig. 11(a)-(b).

C. Light-induced temporal correlations

Having described the ultrafast nature of the dynamics of the interaction between matter and entangled photons, we now focus on the signatures of the hybridization between the two degrees of freedom. We do so by investigating the temporal correlations of the light-stimulated matter degrees of freedom. Temporal correlations carry information about the probability amplitude for the propagation of an excitation in time, and encode the distinctive features of time-energy entangled modes. To see this, we introduce the two-times lesser Green's function [74, 87, 88] for the photon field computed at the position $y = 0$:

$$G_{\text{pht}}(T, \Delta t) \equiv \langle \Phi | \hat{E}^\dagger \left(0, T + \frac{\Delta t}{2} \right) \hat{E} \left(0, T - \frac{\Delta t}{2} \right) | \Phi \rangle. \quad (27)$$

Here, $\hat{E}(y, t)$ and $\hat{E}^\dagger(y, t)$ represent operators in the Heisenberg picture of time evolution, i.e. $\hat{E}(y, t) \equiv e^{i\hat{H}t} \hat{E}(y) e^{-i\hat{H}t}$. The operator $\hat{E}^\dagger(y)$ [$\hat{E}(y)$] represents the creation [annihilation] operator of the electric field $\hat{\mathcal{E}}(y)$ operator, $\hat{\mathcal{E}}(y) \equiv \hat{E}(y) + \hat{E}^\dagger(y)$, with

$$\hat{E}(y) = \frac{1}{\sqrt{L_y}} \sum_k \sqrt{\omega_k} e^{iky} \hat{a}_k. \quad (28)$$

Eq. (27) measures the probability amplitude for destroying a photon excitation at time $T - \Delta t/2$ and creating it back at time $T + \Delta t/2$. By normalizing the Green's function to the joint probability amplitude for counting electric field excitations at times $T + \Delta t/2$ and $T - \Delta t/2$, we obtain the first-order correlation function [74, 88]

$$g_{\text{pht}}^{(1)}(T, \Delta t) = \frac{G_{\text{pht}}(T, \Delta t)}{[\langle \hat{E}^\dagger \hat{E} \rangle (T + \frac{\Delta t}{2}) \langle \hat{E}^\dagger \hat{E} \rangle (T - \frac{\Delta t}{2})]^{1/2}}. \quad (29)$$

When $|g_{\text{pht}}^{(1)}(T, \Delta t)| = 1$, excitations at different times are uncorrelated, namely the probability of creating the excitation at time $T + \Delta t/2$ after having destroyed it at time $T - \Delta t/2$ is exactly equal to the joint probability of counting the excitations at initial and final times.

In order to highlight the temporal correlation of time-energy entangled photons, we compute $g_{\text{pht}}^{(1)}(T, \Delta t)$ in the absence of the light-matter interaction. Fig. 12(a) reports the quantity $|g_{\text{pht}}^{(1)}(T = t_i, \Delta t)|$ for the non-interacting case

as a function of the propagation time Δt and computed at a reference time $T = t_i$ corresponding to the arrival time of the peak of the freely propagating packet at the position $y = 0$ of the 2D material. As expected, for the separable packet we obtain $|g_{\text{pht}}^{(1)}| = 1$, whereas for entangled packets $|g_{\text{pht}}^{(1)}|$ deviates from 1 on a time scale set by the entanglement time τ_{ent} . For strongly entangled packets, $g_{\text{pht}}^{(1)}$ rapidly falls to zero signaling that, due to time-energy entanglement, the photon excitations get strongly correlated in time.

We now introduce the equivalent Green's functions for the matter degrees of freedom and measure the temporal correlation induced by the interaction with the entangled photons. The lesser Green's function for the matter degrees of freedom reads as following:

$$G_{\text{mat}}(T, \Delta t) \equiv \langle \Phi | \hat{b}^\dagger \left(T + \frac{\Delta t}{2} \right) \hat{b} \left(T - \frac{\Delta t}{2} \right) | \Phi \rangle, \quad (30)$$

where, as before, the time dependence of the operators means Heisenberg evolution. Since the ground state of coupled light-matter system does not coincide with the vacuum—see Appendix A—the Green's function (30) contains also information about equilibrium temporal correlations, i.e. in the absence of the driving photon packet. Of course, due to time translation invariance, the equilibrium Green's function depends only on the propagation time $G_{\text{mat}}^{\text{equ}}(\Delta t)$. In order to isolate the modification due to the entangled packet, we subtract the contribution due to the equilibrium correlations, i.e. we introduce the quantity $\delta G_{\text{mat}}(T, \Delta t) \equiv G_{\text{mat}}(T, \Delta t) - G_{\text{mat}}^{\text{equ}}(\Delta t)$, and define the first-order correlation function for the matter degrees of freedom as following:

$$g_{\text{mat}}^{(1)}(T, \Delta t) \equiv \frac{\delta G_{\text{mat}}(T, \Delta t)}{[\delta \langle \hat{b}^\dagger \hat{b} \rangle (T + \frac{\Delta t}{2}) \delta \langle \hat{b}^\dagger \hat{b} \rangle (T - \frac{\Delta t}{2})]^{1/2}}, \quad (31)$$

where $\delta \langle \hat{b}^\dagger \hat{b} \rangle (t) \equiv \langle \hat{b}^\dagger \hat{b} \rangle (t) - \langle \text{GS} | \hat{b}^\dagger \hat{b} | \text{GS} \rangle$ represents the number of matter excitations on top of the ground state. In Fig. 12(b), we show the first-order correlation function $g_{\text{mat}}^{(1)}(T = t_{\text{peak}}, \Delta t)$ as a function of the propagation time Δt and computed at a reference time $T = t_{\text{peak}}$, corresponding to the time at which a peak occurs in the energy absorbed by the matter degrees of freedom. Interestingly, we observe that the first-order correlation functions of the matter degrees of freedom acquires the same qualitative form of the photonic ones. For the case of matter degrees of freedom driven by separable packets, the modulus of $g_{\text{mat}}^{(1)}$ is equal to unity, indicating that the matter excitation created by photons does not display temporal correlations. On the contrary, for entangled incident packets, $|g_{\text{mat}}^{(1)}|$ deviates from one and decays to zero on a time scale which decreases upon increasing the entanglement parameter w_{ent} . This observation provides a clear evidence of the fact that, due to the hybridization between matter and entangled photons, the matter excitation inherits the temporal correlations of the driving

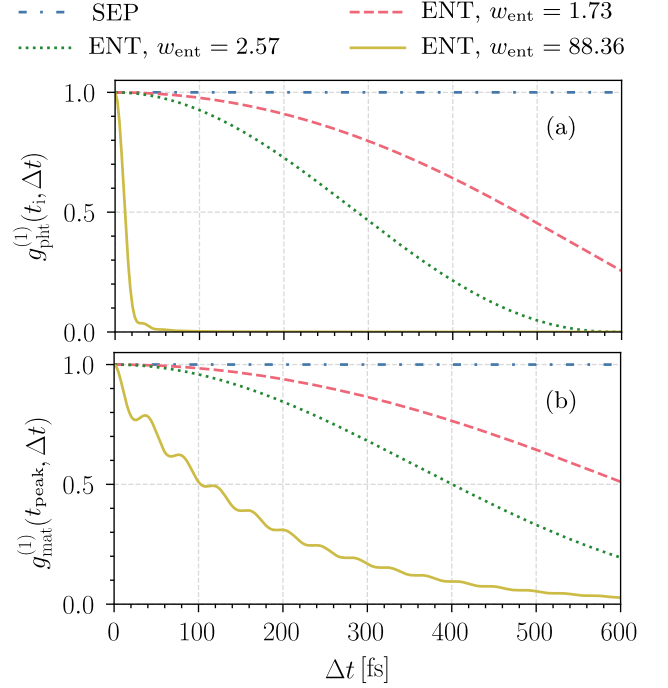


FIG. 12. First-order correlation function, see Eq. (29) and Eq. (31), as a function the propagation time for the photon (a) and matter (b) degrees of freedom. The correlation function is evaluated at the position $y = 0$ of the 2D material and for a reference time $T = t_i$ in panel (a) and $T = t_{\text{peak}}$ in panel (b). The blue dashed-dotted line refers to the case of a separable incoming packet with $\tau_{\text{sep}} \approx 232.71$ fs. The red dashed line to an entangled packet with entanglement parameter $w_{\text{ent}} \approx 1.73$ and $\tau_{\text{ent}} \approx 101.88$ fs. The green dotted line to an entangled packet with $w_{\text{ent}} \approx 2.57$ and $\tau_{\text{ent}} \approx 79.17$ fs. Finally, the yellow solid line to the case of an entangled packet with $w_{\text{ent}} \approx 88.36$ and $\tau_{\text{ent}} \approx 2.63$ fs. All the incident wave packets, entangled and separable, have a fixed FWHM of approximately 556 fs.

pulse.

It is important to stress that the correlation time of the matter excitation is not in a quantitative agreement with the entanglement time of the incident photon packet. This can be understood by considering the fact that the temporal correlation of the light-stimulated matter is the result of the hybridization between the matter and photon degrees of freedom. In particular, the temporal correlations of the incident packets seen in Fig. 12(a), are the result of the superposition of entangled photon modes at all frequencies. On the contrary, the dynamics in the matter collective excitation is dominated by the single resonance frequency ω_0 which hybridizes with all the photon modes. It is therefore not surprising that the light-induced temporal correlations are not in a quantitative agreement with the one contained in the driving field. We leave for future work a more quantitative understanding of the temporal correlations induced by the hybridization between matter and entangled photons.

IV. CONCLUSIONS

We presented a comprehensive study on the effects of light entanglement in the light stimulation of a collective matter excitation. We studied an exactly solvable model in which a single partner of a time-energy entangled pair interacts with a localized matter mode representing an optically active collective excitation of a 2D material. We showed how the time-energy entanglement in the incident photon packets induces qualitative changes in the dynamics of both photon and matter degrees of freedom.

From a purely spectroscopic point of view, our observations show that entangled photons act as an extremely gentle probe of matter which minimizes the absorbed energy and maximizes the number of transmitted photons. On the other hand, from the point of view of the light-induced dynamics, our results show that entanglement driving can effectively control the relevant time scales of the light-matter interaction process. For the photons, this is highlighted by the suppression of the delay between transmission and absorption peaks. For the matter degrees of freedom, entanglement in the driving field suppresses the delay between the arrival of the perturbation and the creation of the excitation, which is formed on a time scale much shorter than the pulse width. We provide an understanding of these behaviors by introducing a representation of entangled photon packets in terms of a superposition of trains of short separable pulses. Overall, our results show how driving matter degrees of freedom with temporally-wide entangled photons embodies features of ultrashort light stimulation.

Our results highlight several future research directions, including, for example, the study of the role of entangled driving in the creation of long-lived light-induced states of matter and the exploration of ultrafast or ballistic energy transport by means of absorption of entangled photons [84, 89, 90]. Moreover, light-induced temporal correlations highlight the intriguing perspective of exploiting entangled photons to control entanglement in matter degrees of freedom, or, possibly, to create states of matter sharing the entanglement properties of the incoming light. Finally, the investigation of the correlations between the two entangled photons represents a natural framework where the theoretical predictions of this Article can be explored experimentally.

ACKNOWLEDGMENTS

M.P. was supported by the MUR - Italian Ministry of University and Research under the “Research projects of relevant national interest - PRIN 2020” - Project No. 2020JLZ52N (“Light-matter interactions and the collective behavior of quantum 2D materials, q-LIMA”) and by the European Union under grant agreement No. 101131579 - Exqiral and No. 873028 - Hydrotronics. Views and opinions expressed are however those of the author(s) only and do not necessarily reflect those of

the European Union or the European Commission. Neither the European Union nor the granting authority can be held responsible for them. M.D. and D.N.B. were supported by the National Science Foundation under grant No. DMR-2210186. G.M. acknowledges support by the MUR - Italian Ministry of University and Research through a “Rita-Levi Montalcini” fellowship.

Appendix A: Hamiltonian Diagonalization.

The Hamiltonian $\hat{\mathcal{H}}$, defined in Eq. (1) of the main text, is quadratic and can therefore be diagonalized by a canonical Bogoliubov transformation.

1. Diagonalization

Here, we briefly summarize the diagonalization procedure following the algorithm proposed by Colpa in Ref. [76].

Consider a quadratic Hamiltonian of the form

$$\hat{\mathcal{H}} = \frac{1}{2} \hat{\Psi}^\dagger H \hat{\Psi}, \quad (\text{A1})$$

where

$$\hat{\Psi} \equiv (\underbrace{\hat{b}, \hat{a}_k, \dots}_{\mathcal{N}}, \hat{b}^\dagger, \hat{a}_k^\dagger, \dots)^T, \quad H^\dagger = H. \quad (\text{A2})$$

We now introduce the operators $\hat{\gamma}_i$ that diagonalize the Hamiltonian. These operators are defined by the relation

$$(\hat{\gamma}_1, \dots, \hat{\gamma}_{\mathcal{N}}, \hat{\gamma}_1^\dagger, \dots, \hat{\gamma}_{\mathcal{N}}^\dagger)^T \equiv \hat{\Omega} = \mathcal{W} \hat{\Psi}. \quad (\text{A3})$$

The transformation matrix \mathcal{W} is *para-unitary*, satisfying

$$\mathcal{W}^\dagger \tau^z \mathcal{W} = \tau^z, \quad \tau^z \equiv \begin{pmatrix} \mathbb{1} & 0 \\ 0 & -\mathbb{1} \end{pmatrix}, \quad (\text{A4})$$

which ensures the conservation of the bosonic canonical commutation relations for the $\hat{\gamma}$ operators

$$[\hat{\gamma}_a, \hat{\gamma}_{a'}^\dagger] = \delta_{a,a'}. \quad (\text{A5})$$

It follows that

$$\hat{\mathcal{H}} = \frac{1}{2} \hat{\Omega}^\dagger \epsilon \hat{\Omega}, \quad (\text{A6})$$

where

$$(\mathcal{W}^\dagger)^{-1} H \mathcal{W}^{-1} \equiv \epsilon, \quad \epsilon_{ab} = \epsilon_a \delta_{a,b}, \quad (\text{A7a})$$

$$\epsilon = (\epsilon_1, \dots, \epsilon_{\mathcal{N}}, \epsilon_1, \dots, \epsilon_{\mathcal{N}})^T. \quad (\text{A7b})$$

and $\delta_{a,b}$ is the Kronecker delta.

To find \mathcal{W}^{-1} , we first find the Cholesky decomposition

$$H = K^\dagger K. \quad (\text{A8})$$

Then, we define

$$\mathcal{U} \equiv K\mathcal{W}^{-1}\epsilon^{-1/2}, \quad \mathcal{U}\mathcal{U}^\dagger = 1. \quad (\text{A9})$$

Furthermore, the unitary matrix \mathcal{U} diagonalizes $K\tau^z K^\dagger$. Indeed,

$$\begin{aligned} \mathcal{U}^\dagger K\tau^z K^\dagger \mathcal{U} &= \epsilon^{1/2} \tau^z \epsilon^{1/2} \\ &= \text{diag}(\epsilon_1, \epsilon_2, \dots, \epsilon_N, -\epsilon_1, -\epsilon_2, \dots, -\epsilon_N). \end{aligned} \quad (\text{A10})$$

We can now evaluate \mathcal{W}^{-1} from Eq. (A9). Furthermore, we define $(\mathbf{u}_i, \mathbf{v}_i)^T$ as the i -th column of \mathcal{W}^{-1} , where \mathbf{u}_i and \mathbf{v}_i are \mathcal{N} -component vectors. Finally, we take the first \mathcal{N} columns $(\mathbf{u}_i, \mathbf{v}_i)^T$ of the matrix \mathcal{W}^{-1} and redefine

$$\mathcal{W}^{-1} \equiv \begin{pmatrix} \mathbf{u}_1 & \mathbf{u}_2 & \dots & \mathbf{u}_N & \mathbf{v}_1^* & \mathbf{v}_2^* & \dots & \mathbf{v}_N^* \\ \mathbf{v}_1 & \mathbf{v}_2 & \dots & \mathbf{v}_N & \mathbf{u}_1^* & \mathbf{u}_2^* & \dots & \mathbf{u}_N^* \end{pmatrix}, \quad (\text{A11})$$

where \mathbf{u}^* and \mathbf{v}^* are the complex conjugates of \mathbf{u} and \mathbf{v} . The matrix \mathcal{W}^{-1} is now para-unitary and diagonalizes H .

2. Time evolution

Introducing the vector

$$\hbar \mathbf{f} \equiv (\epsilon_1, \dots, \epsilon_N, -\epsilon_1, \dots, -\epsilon_N)^T, \quad (\text{A12})$$

we write

$$[\hat{\mathcal{H}}, \hat{\Omega}_i] = -f_i \hat{\Omega}_i \implies \hat{\Omega}_i(t) = e^{-if_i t} \hat{\Omega}_i(t=0). \quad (\text{A13})$$

We now show how to use Colpa's algorithm to evaluate the relevant expectation values. We are interested in expectation values that contain operators such as

$$\hat{a}_\mu(t) e^{ik_\mu y}, \quad \hat{b}(t), \quad (\text{A14})$$

and the corresponding Hermitian counterparts. We introduce the $2\mathcal{N} \times \mathcal{N}$ matrix \mathcal{P} defined as

$$\mathcal{P}_{i\alpha}(t, y) \equiv e^{-if_i t} [\mathcal{W}^{-1}]_{i\alpha}^T e^{ik_\alpha y}. \quad (\text{A15})$$

Using Eq. A15, we can write

$$\begin{aligned} \langle \hat{E}^{(-)}(t', y') \hat{E}^{(+)}(t, y) \rangle &= \frac{1}{L_y} \sum_{\{\alpha, \beta\}=2}^{\mathcal{N}} e^{i(k_\beta y - k_\alpha y')} \sqrt{\omega_\alpha \omega_\beta} \langle \hat{a}_\alpha^\dagger(t') \hat{a}_\beta(t) \rangle \\ &= \sum_{\{\alpha, \beta\}=2}^{\mathcal{N}} \sum_{\{i, j\}=1}^{2\mathcal{N}} \frac{\sqrt{\omega_\alpha \omega_\beta}}{L_y} \mathcal{P}_{\alpha i}^\dagger(t', y') \langle \hat{\Omega}_i^\dagger \hat{\Omega}_j \rangle \mathcal{P}_{j\beta}(t, y), \end{aligned} \quad (\text{A16})$$

and

$$\langle \hat{b}^\dagger(t') \hat{b}(t) \rangle = \sum_{\{i, j\}=1}^{2\mathcal{N}} \mathcal{P}_{1i}^\dagger(t', 0) \langle \hat{\Omega}_i^\dagger \hat{\Omega}_j \rangle \mathcal{P}_{j,1}(t, 0), \quad (\text{A17})$$

where $\langle \hat{\Omega}_i \hat{\Omega}_j \rangle$ is evaluated at the initial time. All other relevant expectation values can be calculated in a similar manner.

Details regarding the calculation of the expectation value $\langle \hat{\Omega}_i \hat{\Omega}_j \rangle$ at initial time are provided in Appendix B.

Appendix B: Entangled and separable photon state initialization on the ground state

The interaction Hamiltonian, defined in Eqs. (2a)-(2b) of the main text, modifies the ground state of the total Hamiltonian (1). Consequently the vacuum $|0\rangle$ for the bare annihilation photon and matter operators i.e., $\hat{a}_k|0\rangle = \hat{b}|0\rangle = 0$, is no longer an eigenstate of the total Hamiltonian (1). The first consequence is that the resonant frequency of the material is shifted from ω_0 to ω_* . This effect is discussed in detail in Appendix C. The second consequence, discussed further in this Appendix, is crucial for accurate numerical simulations.

Initializing the photon state $|\Phi\rangle$ relative to the interacting ground state $|\text{GS}\rangle$ is necessary to ensure accurate numerical simulations and prevent artifacts in the photon dynamics. Specifically, if $|\Phi\rangle$ is constructed relative to the bare vacuum $|0\rangle$, photon wave packets traveling in opposite directions will be generated at the initial time from the material. This issue arises not from the unitary dynamics itself (which, for a given initial state, is always correct up to numerical precision) but from the fact that $|0\rangle$ is not an eigenstate of the total Hamiltonian. Therefore, even though the unitary dynamics is correct, constructing $|\Phi\rangle$ relative to $|0\rangle$ implies the system is out of equilibrium at the initial time. This is what we term *artifacts in photon dynamics*. Physically, if the initial wave packet is initialized very far from the material, the choice of initialization relative to the bare vacuum or relative to the interacting ground state should be equivalent. However, such an ideal condition can only be achieved approximately in numerical simulations, and we find that only initialization relative to the interacting ground state $|\text{GS}\rangle$ avoids these simulation artifacts. Here, we explicitly describe how the photon state $|\Phi\rangle$ is initialized relative to $|\text{GS}\rangle$.

A generic two-photon state $|\Phi\rangle$, defined relative to the interacting ground state $|\text{GS}\rangle$ of the total Hamiltonian, can be written as

$$|\Phi\rangle \equiv \sum_{\mu, \nu} \phi_{\mu\nu} \hat{a}_\mu^\dagger \hat{a}_\nu^\dagger |\text{GS}\rangle = \sum_{i, j} \mathcal{K}_{ij}^\dagger \hat{\Omega}_i^\dagger \hat{\Omega}_j^\dagger |\text{GS}\rangle, \quad (\text{B1})$$

where the matrix \mathcal{K} is defined as

$$\mathcal{K} \equiv [\mathcal{W}^{-1}]^T \phi^\dagger \mathcal{W}^{-1} \equiv \begin{pmatrix} \mathcal{K}_1 & \mathcal{K}_2 \\ \mathcal{K}_3 & \mathcal{K}_4 \end{pmatrix}, \quad (\text{B2})$$

and $\hat{\Omega}$ is defined as

$$\hat{\Omega} = (\hat{\gamma}_1, \dots, \hat{\gamma}_N, \hat{\gamma}_1^\dagger, \dots, \hat{\gamma}_N^\dagger)^T, \quad (\text{B3})$$

where $|\text{GS}\rangle$ is the vacuum for the $\hat{\gamma}$ operators that diagonalize the total Hamiltonian and \mathcal{W}^{-1} is the transformation matrix, see App. A.

The state $|\Phi\rangle$ is normalized by imposing $\langle \Phi | \Phi \rangle = 1$, which leads to the condition

$$\langle \Phi | \Phi \rangle = |\text{Tr}[\mathcal{K}_2]|^2 + \text{Tr}[\mathcal{K}_1 \mathcal{K}_1^*] + \text{Tr}[\mathcal{K}_1 \mathcal{K}_1^\dagger] = 1, \quad (\text{B4})$$

where we have used Wick's theorem.

We now calculate the expectation values

$$\mathcal{M}_{\ell n} \equiv \langle \Phi | \hat{\Omega}_\ell^\dagger \hat{\Omega}_n | \Phi \rangle - \langle \text{GS} | \hat{\Omega}_\ell^\dagger \hat{\Omega}_n | \text{GS} \rangle. \quad (\text{B5})$$

In the following, we assume the Einstein summation convention over repeated indices. We also adopt the notation used in the main text

$$\langle \quad \rangle_0 \equiv \langle \text{GS} | \quad | \text{GS} \rangle, \quad \langle \quad \rangle \equiv \langle \Phi | \quad | \Phi \rangle - \langle \text{GS} | \quad | \text{GS} \rangle. \quad (\text{B6})$$

Applying Wick's theorem to the expectation value (B5) yields

$$\begin{aligned} \mathcal{M}_{\ell n} &= \langle \hat{\Omega}_\ell^\dagger \hat{\Omega}_n \rangle = \mathcal{K}_{ij} \mathcal{K}_{sp}^\dagger \langle \hat{\Omega}_i \hat{\Omega}_j \hat{\Omega}_\ell^\dagger \hat{\Omega}_n \hat{\Omega}_s^\dagger \hat{\Omega}_p^\dagger \rangle_0 \\ &= (\mathcal{K}_{ij} \mathcal{K}_{sp}^\dagger) \left(\langle \hat{\Omega}_i \hat{\Omega}_\ell^\dagger \rangle_0 \langle \hat{\Omega}_j \hat{\Omega}_n \hat{\Omega}_s^\dagger \hat{\Omega}_p^\dagger \rangle_0 \right. \\ &\quad + \langle \hat{\Omega}_j \hat{\Omega}_\ell^\dagger \rangle_0 \langle \hat{\Omega}_i \hat{\Omega}_n \hat{\Omega}_s^\dagger \hat{\Omega}_p^\dagger \rangle_0 + \langle \hat{\Omega}_\ell^\dagger \hat{\Omega}_s^\dagger \rangle_0 \langle \hat{\Omega}_i \hat{\Omega}_j \hat{\Omega}_n \hat{\Omega}_p^\dagger \rangle_0 \\ &\quad \left. + \langle \hat{\Omega}_\ell^\dagger \hat{\Omega}_p^\dagger \rangle_0 \langle \hat{\Omega}_i \hat{\Omega}_j \hat{\Omega}_n \hat{\Omega}_s^\dagger \rangle_0 \right), \quad (\text{B7}) \end{aligned}$$

which can be written in the block matrix form

$$\mathcal{M} = \begin{pmatrix} \Delta & (\mathcal{K}_1 + \mathcal{K}_1^T) \text{Tr}[\mathcal{K}_2]^* \\ (\mathcal{K}_1^\dagger + \mathcal{K}_1^*) \text{Tr}[\mathcal{K}_2] & \Delta^* \end{pmatrix}, \quad (\text{B8})$$

where we have introduced the matrix

$$\Delta \equiv \mathcal{K}_1 \mathcal{K}_1^\dagger + \mathcal{K}_1 \mathcal{K}_1^* + \mathcal{K}_1^T \mathcal{K}_1^\dagger + \mathcal{K}_1^T \mathcal{K}_1^*. \quad (\text{B9})$$

The calculation for an initial separable two-photon Fock state follows directly by setting $\phi_{\mu\nu} = \psi_\mu \varphi_\nu$ in the above expressions.

Appendix C: Spontaneous Decay Rate and Dressed Matter Resonant Frequency

In this Appendix, we present the analytical and numerical evaluation of the spontaneous decay rate Γ defined in Sec. III A of the main text. We also evaluate numerically the dressed resonance frequency ω_* from the transmission coefficient $T(\omega)$ defined in Eq. (12).

1. Analytical calculation

To calculate the decay rate, we use the Fermi golden rule

$$\Gamma = \frac{2\pi}{\hbar} |\langle i | \hat{\mathcal{H}}_{\text{int}} | f \rangle|^2 \rho(E = E_0), \quad (\text{C1})$$

where $\hat{\mathcal{H}}_{\text{int}}$ is a suitable interaction Hamiltonian, $\rho(E = E_0)$ is the density of final states at the transition energy E_0 , and $|i\rangle$ and $|f\rangle$ are the initial and final states, respectively.

As far as the interaction Hamiltonian is concerned, we take

$$\hat{\mathcal{H}}_{\text{int}} \equiv -i\hbar\omega_0 \tilde{g} \sum_k \frac{1}{\sqrt{\omega_k}} (\hat{b} \hat{a}_k^\dagger + \hat{b}^\dagger \hat{a}_k), \quad (\text{C2})$$

which connects initial and final states with the same energy. The interaction Hamiltonian (C2) can be obtained from the full light-matter interaction $\hat{\mathcal{H}}_{\text{mat-pht}}$ in the rotating-wave approximation [74].

To calculate the spontaneous decay rate, we consider the transition from the initial state

$$|i\rangle \equiv |0_{\text{photons}}; 1_{\text{phonons}}\rangle, \quad (\text{C3})$$

which contains a single phonon with energy E_0 , to the final state

$$|f\rangle \equiv |1_{\text{photons}, \omega_0}; 0_{\text{phonons}}\rangle, \quad (\text{C4})$$

which contains a single photon with energy $\hbar\omega_0 = E_0$. It follows that

$$|\langle i | \hat{\mathcal{H}}_{\text{interaction}} | f \rangle|^2 = (\hbar\omega_0 \tilde{g})^2 = \frac{\hbar^2 \omega_0 \tilde{g}^2 \alpha \pi c}{L_y}. \quad (\text{C5})$$

We now calculate the density of states $\rho(E)$ for the photons. If $\mathfrak{N}_{\text{pht}}$ is the number of photon modes, we can write

$$d\mathfrak{N}_{\text{pht}} = \frac{dk_y}{2\pi/L_y} = \frac{L_y}{\hbar c \pi} dE \equiv \rho(E) dE, \quad (\text{C6})$$

which implies

$$\rho(E) = \frac{L_y}{\hbar c \pi}. \quad (\text{C7})$$

Finally, substituting Eq. (C5) and Eq. (C7) into the Fermi golden rule Eq. (C1), gives the spontaneous decay rate

$$\Gamma = 2\omega_0 \pi \tilde{g}^2 \alpha \approx 6.97 \text{ THz}, \quad (\text{C8})$$

where in the last equation we used $\hbar\omega_0 = 100 \text{ meV}$ and $\tilde{g} = 1$.

2. Numerical estimation

Here, we estimate the spontaneous decay rate from the transmission coefficient $T(\omega)$ defined in Eq. (12). In Fig. 13, we show numerical data for the squared magnitude of the transmission coefficient. The data are fitted using the model function

$$T(\omega) = \frac{\omega - \omega_*}{\omega - \omega_* + i\Gamma/2}, \quad (\text{C9})$$

whose form is based on Eq. (12) in the main text. The fit yields the parameters $\omega_* = (1.0082 \pm 0.0001) \omega_0$ and $\Gamma = (4.31 \pm 0.03) \text{ THz}$, evaluated assuming $\hbar\omega_0 = 100 \text{ meV}$.

Appendix D: Entanglement Entropy

Here, we briefly explain how to compute the von Neumann entanglement entropy introduced in Sec. II. More details can be found in Ref. [79].

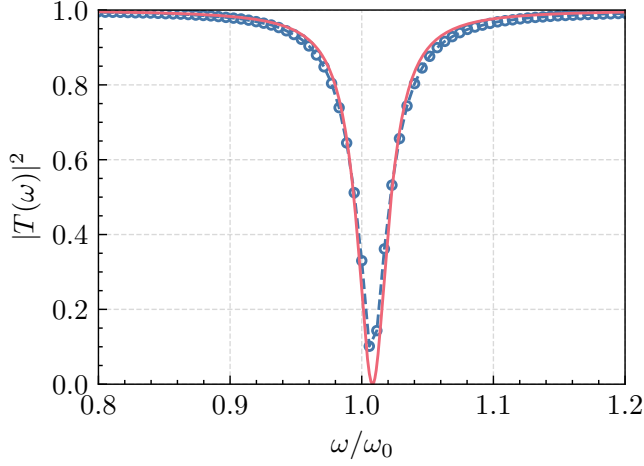


FIG. 13. Absolute square value of the coefficient transmission. The blue points are the numerical data, while the solid orange line is evaluated from a fit with the model function Eq. (C9)

Consider a generic two-mode Fock state

$$|\Phi\rangle \equiv \sum_{\mu\nu} \phi_{\mu\nu} \hat{a}_\mu^\dagger \hat{a}_\nu^\dagger |0\rangle, \quad \langle\Phi|\Phi\rangle = 1. \quad (\text{D1})$$

We define two matrix kernels

$$K_1 \equiv \phi\phi^\dagger, \quad K_2 \equiv \phi^\dagger\phi, \quad (\text{D2})$$

and introduce the orthonormal eigenvectors $\psi_\mu^{(n)}$ and $\varphi_\mu^{(n)}$, satisfying

$$K_1 \psi_\mu^{(n)} = \lambda_n \psi_\mu^{(n)}, \quad K_2 \varphi_\mu^{(n)} = \lambda_n \varphi_\mu^{(n)}, \quad (\text{D3})$$

where the eigenvalues λ_n are real and non-negative. The Schmidt modes are then introduced as

$$\hat{A}_n \equiv \sum_\mu \psi_\mu^{(n)} \hat{a}_\mu, \quad \hat{B}_n \equiv \sum_\mu \varphi_\mu^{(n)} \hat{a}_\mu, \quad (\text{D4})$$

so that the two-mode Fock state can be written as a sum of factorized states (Schmidt decomposition)

$$|\Phi\rangle = \sum_n \lambda_n \hat{A}_n^\dagger \hat{B}_n^\dagger |0\rangle. \quad (\text{D5})$$

The von Neumann entanglement entropy is then evaluated as

$$E_N = - \sum_n \lambda_n^2 \log(\lambda_n^2). \quad (\text{D6})$$

Appendix E: Analytical Model

In this Appendix, we derive the equations for the analytical model introduced in Sec. III A.

For definitions of special functions and standard integrals and sums, we refer to Ref. [91]. Furthermore, we use the notation $\partial_x^j f \equiv \frac{\partial^j f}{\partial x^j}$ to denote the j -th derivative of a function $f(x)$ with respect to x .

1. Normalization constant

We first calculate the normalization constant N that appears in the function $\psi(\omega)$ defined in Eq. (17) of the main text. To calculate N , we focus on the non-interacting case, which implies $T(\omega) = 1$. In this limit, the wavefunction $\Psi_0(\tau)$ —see Eq. (16)—simplifies to

$$\Psi_0^{(0)}(\tau) = N e^{-\tau^2/2\tau_+^2}. \quad (\text{E1})$$

where the superscript (0), like in the main text, refers to the limit $T(\omega) \rightarrow 1$.

The j -th wave function $\Psi_j(\tau)$ is proportional to the j -th momentum $\langle\langle\omega^j\rangle\rangle(\tau)$ —both in the interacting and non-interacting case—which can be written as

$$\langle\langle\omega^j\rangle\rangle(\tau) = i^j \partial_\tau^j \Psi_0(\tau). \quad (\text{E2})$$

We define the dimensionless variable $\eta \equiv \tau/\tau_+$, which implies

$$\partial_\tau^j \Psi_0^{(0)} = \tau_+^{-j} \partial_\eta^j \Psi_0^{(0)} = N e^{-\eta^2/2} \frac{(-1)^j}{\tau_+^j 2^{j/2}} H_j\left(\frac{\eta}{\sqrt{2}}\right), \quad (\text{E3})$$

where we used the definition of the Hermite polynomials

$$H_j(\eta) = (-1)^j e^{\eta^2} \partial_\eta^j e^{-\eta^2}. \quad (\text{E4})$$

For the elementary photon densities $n_j^{(0)}(\tau)$ defined in Eq. (22) of the main text, it thus follows

$$n_j^{(0)}(\tau) = |\Psi_j^{(0)}(\tau)|^2 = e^{-\tau^2/\tau_+^2} H_j^2\left(\frac{\tau}{\sqrt{2}\tau_+}\right) \left(\frac{\tau_-}{\tau_+}\right)^{2j} \frac{N^2}{j! 2^j}, \quad (\text{E5})$$

where

$$\Psi_j^{(0)}(\tau) = \frac{\tau_-^j}{\sqrt{j!}} \langle\langle\omega^j\rangle\rangle^{(0)}(\tau), \quad (\text{E6})$$

as defined in Eq. (19) of the main text.

We define

$$\begin{aligned} I_j &\equiv \int d\eta (\partial_\eta^j \Psi_0^{(0)}) (\partial_\eta^j \Psi_0^{(0)}) \\ &= (-1)^j \int d\eta (\partial_\eta^{2j} \Psi_0^{(0)}(\eta)) \Psi_0^{(0)}(\eta) \\ &= \frac{N^2 (-1)^j \sqrt{2}}{2^j} \int d\eta e^{-2\eta^2} H_{2j}(\eta), \end{aligned} \quad (\text{E7})$$

where the second equality follows from repeated integration by parts. Using the relation

$$\begin{aligned} \sum_{j=0}^{+\infty} \int d\eta e^{-2\eta^2} H_j(\eta) \frac{t^j}{j!} &= \int d\eta e^{2\eta t - t^2 - 2\eta^2} \\ &= e^{-t^2/2} \sqrt{\frac{\pi}{2}} = \sqrt{\frac{\pi}{2}} \sum_{j=0}^{+\infty} \frac{(-1)^j}{2^j j!} t^{2j} \end{aligned} \quad (\text{E8})$$

we find

$$\int d\eta e^{-2\eta^2} H_{2j}(\eta) = \sqrt{\frac{\pi}{2}} \frac{(-1)^j (2j)!}{2^j j!} \quad (\text{E9})$$

and thus

$$I_j = \frac{N^2(-1)^j\sqrt{2}}{2^j} \int d\eta e^{-2\eta^2} H_{2j}(\eta) = \frac{N^2\sqrt{\pi}(2j)!}{2^{2j}j!}. \quad (\text{E10})$$

We can now calculate the total number of photons carried by the j -th elementary photon density—Eq. (24)—by performing the integration

$$N_j^{(0)} = c\tau_+ \int d\eta n_j^{(0)}(\eta) = N^2 c\tau_+ \sqrt{\pi} \binom{2j}{j} \left(\frac{\tau_-}{2\tau_+}\right)^{2j}. \quad (\text{E11})$$

The total number of photons is obtained by summing Eq. (E11) over j i.e.,

$$N^{(0)} = \sum_{j=0}^{+\infty} c\tau_+ \int d\eta n_j^{(0)}(\eta) = \frac{N^2 c\tau_+ \sqrt{\pi}}{\sqrt{1 - (\tau_-/\tau_+)^2}}, \quad (\text{E12})$$

with $(\tau_-/\tau_+)^2 < 1$. We normalize the state to contain a single photon ($N^{(0)} = 1$) by imposing

$$N^2 = \sqrt{1 - (\tau_-/\tau_+)^2} / (c\tau_+ \sqrt{\pi}). \quad (\text{E13})$$

2. Transmitted wave packet

We now focus on the transmitted separable wave packet. We evaluate $\Psi_0(\tau)$ defined in Eq. (17) of the main text, including the effect of the transmission coefficient, i.e.

cient, i.e.

$$\begin{aligned} \Psi_0(\tau) &= \frac{N\tau_+}{\sqrt{2\pi}} \int_{-\infty}^{+\infty} d\omega e^{-\frac{\omega^2\tau_+^2}{2} - i\omega\tau} \frac{\omega}{\omega + i\Gamma/2} \\ &= N e^{-\frac{\tau_-^2}{2\tau_+^2} - iN\Gamma} \int_{-\infty}^{+\infty} d\omega e^{-\frac{\omega^2\tau_+^2}{2} - i\omega\tau} \frac{1}{\omega + i\Gamma/2}. \end{aligned} \quad (\text{E14})$$

We introduce the integral representation of the denominator

$$\frac{i}{\omega + i\Gamma/2} = \int_{-\infty}^{+\infty} d\lambda e^{-i\lambda\omega + \Gamma\lambda/2} \Theta(-\lambda), \quad (\text{E15})$$

where $\Theta(\lambda)$ is the Heaviside distribution. Substituting Eq. (E15) into Eq. (E14), and performing the Gaussian integral over ω , we rewrite

$$\begin{aligned} & -i\frac{\Gamma}{2} \int_{-\infty}^{+\infty} d\omega e^{-\omega^2\tau_+^2/2 - i\omega\tau} \frac{1}{\omega + i\Gamma/2} \\ &= -\frac{\Gamma}{2} \int_{-\infty}^{+\infty} d\lambda \int_{-\infty}^{+\infty} d\omega \Theta(-\lambda) e^{-\frac{\omega^2\tau_+^2}{2} - i\omega(\tau+\lambda) + \frac{\Gamma\lambda}{2}} \\ &= -\frac{\Gamma}{2} \int_{-\infty}^{+\infty} d\lambda e^{\frac{\Gamma\lambda}{2} - \frac{(\lambda+\tau)^2}{2\tau_+^2}} \Theta(-\lambda) \\ &= \sqrt{\frac{\pi}{2}} \frac{\Gamma}{2} \tau_+ e^{\frac{\Gamma^2\tau_+^2}{8} - \frac{\Gamma\tau}{2}} \left(\text{Erf} \left[\frac{\Gamma\tau_+}{2\sqrt{2}} - \frac{\tau}{\sqrt{2}\tau_+} \right] - 1 \right), \end{aligned} \quad (\text{E16})$$

which implies

$$\begin{aligned} \Psi_0(\tau) &= N \left(e^{-\tau^2/2\tau_+^2} \right. \\ &\quad \left. + \sqrt{\frac{\pi}{2}} \Gamma\tau_+ e^{\Gamma^2\tau_+^2/2 - \Gamma\tau} \left(\text{Erf}[(\Gamma\tau_+ - \tau/\tau_+)/\sqrt{2}] - 1 \right) \right) \end{aligned} \quad (\text{E17})$$

The transmitted elementary photon density $n_j(\tau)$ can then be evaluated as

$$n_j(\tau) = |\Psi_j(\tau)|^2 = \left| \langle \omega^j \rangle(\tau) \right|^2 \frac{\tau_-^{2j}}{j!} = \left| \partial_\tau^j \Psi_0 \right|^2 \frac{\tau_-^{2j}}{j!}. \quad (\text{E18})$$

-
- [1] D. Afanasiev, J. R. Hortensius, B. A. Ivanov, A. Sasani, E. Bousquet, Y. M. Blanter, R. V. Mikhaylovskiy, A. V. Kimel, and A. D. Caviglia, Ultrafast control of magnetic interactions via light-driven phonons, *Nat. Mater.* **20**, 607 (2021).
 - [2] S. Fava, G. De Vecchi, G. Jotzu, M. Buzzi, T. Gebert, Y. Liu, B. Keimer, and A. Cavalleri, Magnetic field expulsion in optically driven $\text{YBa}_2\text{Cu}_3\text{O}_{6.48}$, *Nature* **632**, 75 (2024).
 - [3] M. Mitrano, A. Cantaluppi, D. Nicoletti, S. Kaiser, A. Perucchi, S. Lupi, P. Di Pietro, D. Pontiroli, M. Riccò, S. R. Clark, D. Jaksch, and A. Cavalleri, Possible light-induced superconductivity in K_3C_{60} at high temperature, *Nature* **530**, 461 (2016).

- [4] T. F. Nova, A. S. Disa, M. Fechner, and A. Cavalleri, Metastable ferroelectricity in optically strained SrTiO_3 , *Science* **364**, 1075 (2019).
- [5] X. Li, T. Qiu, J. Zhang, E. Baldini, J. Lu, A. M. Rappe, and K. A. Nelson, Terahertz field-induced ferroelectricity in quantum paraelectric SrTiO_3 , *Science* **364**, 1079 (2019).
- [6] F. J. Garcia-Vidal, C. Ciuti, and T. W. Ebbesen, Manipulating matter by strong coupling to vacuum fields, *Science* **373**, 6551 (2021).
- [7] C. Genet, J. Faist, and T. Ebbesen, Inducing new material properties with hybrid light-matter states, *Phys. Today* **74**, 42 (2021).
- [8] H. Hübener, U. De Giovannini, C. Schäfer, J. Andberger, M. Ruggenthaler, J. Faist, and A. Rubio, En-

- gineering quantum materials with chiral optical cavities, *Nat. Mater.* **20**, 438 (2021).
- [9] J. Bloch, A. Cavalleri, V. Galitski, M. Hafezi, and A. Rubio, Strongly correlated electron–photon systems, *Nature* **606**, 41 (2022).
 - [10] F. Schlawin, D. M. Kennes, and M. A. Sentef, Cavity quantum materials, *Appl. Phys. Rev.* **9**, 011312 (2022).
 - [11] H. Hübener, E. Viñas Boström, M. Claassen, L. Simone, and A. Rubio, Quantum materials engineering by structured cavity vacuum fluctuations, *Mater. Quantum. Technol.* **4**, 023002 (2024).
 - [12] G. Scalari, C. Maissen, D. Turcinková, D. Hagenmüller, S. De Liberato, C. Ciuti, C. Reichl, D. Schuh, W. Wegscheider, M. Beck, and J. Faist, Ultrastrong coupling of the cyclotron transition of a 2D electron gas to a THz metamaterial, *Science* **335**, 1323 (2012).
 - [13] V. M. Muravev, P. A. Gusikhin, I. V. Andreev, and I. V. Kukushkin, Ultrastrong coupling of high-frequency two-dimensional cyclotron plasma mode with a cavity photon, *Phys. Rev. B* **87**, 045307 (2013).
 - [14] C. Maissen, G. Scalari, F. Valmorra, M. Beck, J. Faist, S. Cibella, R. Leoni, C. Reichl, C. Charpentier, and W. Wegscheider, Ultrastrong coupling in the near field of complementary split-ring resonators, *Phys. Rev. B* **90**, 205309 (2014).
 - [15] S. Smolka, W. Wuester, F. Haupt, S. Faelt, W. Wegscheider, and A. Imamoglu, Cavity quantum electrodynamics with many-body states of a two-dimensional electron gas, *Science* **346**, 332 (2014).
 - [16] J. Keller, G. Scalari, S. Cibella, C. Maissen, F. Appugliese, E. Giovine, R. Leoni, M. Beck, and J. Faist, Few-electron ultrastrong light-matter coupling at 300 GHz with nanogap hybrid LC microcavities, *Nano Lett.* **17**, 7410 (2017).
 - [17] G. L. Paravicini-Bagliani, F. Appugliese, E. Richter, F. Valmorra, J. Keller, M. Beck, N. Bartolo, C. Rössler, T. Ihn, K. Ensslin, C. Ciuti, G. Scalari, and J. Faist, Magneto-transport controlled by Landau polariton states, *Nat. Phys.* **15**, 186 (2019).
 - [18] F. Appugliese, J. Enkner, G. L. Paravicini-Bagliani, M. Beck, R. Christian, W. Werner, S. Giacomo, C. Cristiano, and F. Jérôme, Breakdown of topological protection by cavity vacuum fields in the integer quantum Hall effect, *Science* **375**, 1030 (2022).
 - [19] G. Jarc, S. Y. Mathengattil, A. Montanaro, F. Giusti, E. M. Rigoni, R. Sergo, F. Fassioli, S. Winnerl, S. Dal Zilio, D. Mihailovic, P. Prelovšek, M. Eckstein, and D. Fausti, Cavity-mediated thermal control of metal-to-insulator transition in 1T-TaS₂, *Nature* **622**, 487 (2023).
 - [20] B. S. Y. Kim, A. J. Sternbach, M. S. Choi, Z. Sun, F. L. Ruta, Y. Shao, A. S. McLeod, L. Xiong, Y. Dong, T. S. Chung, A. Rajendran, S. Liu, A. Nipane, S. H. Chae, A. Zangiabadi, X. Xu, A. J. Millis, P. J. Schuck, C. R. Dean, J. C. Hone, and D. N. Basov, Ambipolar charge-transfer graphene plasmonic cavities, *Nat. Mater.* **22**, 838 (2023).
 - [21] G. Mazza and A. Georges, Superradiant quantum materials, *Phys. Rev. Lett.* **122**, 017401 (2019).
 - [22] G. M. Andolina, F. M. D. Pellegrino, V. Giovannetti, A. H. MacDonald, and M. Polini, Cavity quantum electrodynamics of strongly correlated electron systems: a no-go theorem for photon condensation, *Phys. Rev. B* **100**, 121109(R) (2019).
 - [23] G. M. Andolina, F. M. D. Pellegrino, V. Giovannetti, A. H. MacDonald, and M. Polini, Theory of photon condensation in a spatially varying electromagnetic field, *Phys. Rev. B* **102**, 125137 (2020).
 - [24] G. Mazza and M. Polini, Hidden excitonic quantum states with broken time-reversal symmetry, *Phys. Rev. B* **108**, L241107 (2023).
 - [25] I. Amelio, L. Korosec, I. Carusotto, and G. Mazza, Optical dressing of the electronic response of two-dimensional semiconductors in quantum and classical descriptions of cavity electrodynamics, *Phys. Rev. B* **104**, 235120 (2021).
 - [26] G. M. Andolina, F. M. D. Pellegrino, A. Mercurio, O. Di Stefano, M. Polini, and S. Savasta, A non-perturbative no-go theorem for photon condensation in approximate models, *Eur. Phys. J. Plus* **137**, 1348 (2022).
 - [27] G. M. Andolina, A. De Pasquale, F. M. D. Pellegrino, I. Torre, F. H. L. Koppens, and M. Polini, Amperean superconductivity cannot be induced by deep subwavelength cavities in a two-dimensional material, *Phys. Rev. B* **109**, 104513 (2024).
 - [28] R. Riolo, A. Tomadin, G. Mazza, R. Asgari, A. H. MacDonald, and M. Polini, Tuning Fermi liquids with subwavelength cavities, [arXiv:2403.20067](https://arxiv.org/abs/2403.20067).
 - [29] A. Aspect, J. Dalibard, and G. Roger, Experimental test of Bell’s inequalities using time-varying analyzers, *Phys. Rev. Lett.* **49**, 1804 (1982).
 - [30] Z. Y. Ou and L. Mandel, Violation of Bell’s inequality and classical probability in a two-photon correlation experiment, *Phys. Rev. Lett.* **61**, 50 (1988).
 - [31] V. Giovannetti, S. Lloyd, and L. Maccone, Quantum-enhanced measurements: beating the standard quantum Limit, *Science* **306**, 1330 (2004).
 - [32] V. Giovannetti, S. Lloyd, and L. Maccone, Quantum metrology, *Phys. Rev. Lett.* **96**, 010401 (2006).
 - [33] P. Moreau, E. Toninelli, T. Gregory, and M. J. Padgett, Imaging with quantum states of light, *Nat. Rev. Phys.* **1**, 367 (2019).
 - [34] S. Slussarenko and G. J. Pryde, Photonic quantum information processing: a concise review, *Appl. Phys. Rev.* **6**, 041303 (2019).
 - [35] J. Wang, F. Sciarrino, A. Laing, and M. G. Thompson, Integrated photonic quantum technologies, *Nat. Photon.* **14**, 273 (2020).
 - [36] K. E. Dorfman, F. Schlawin, and S. Mukamel, Nonlinear optical signals and spectroscopy with quantum light, *Rev. Mod. Phys.* **88**, 045008 (2016).
 - [37] S. Szoke, H. Liu, B. P. Hickam, M. He, and S. K. Cushing, Entangled light–matter interactions and spectroscopy, *J. Mater. Chem. C* **8**, 10732 (2020).
 - [38] S. Mukamel, M. Freyberger, W. Schleich, M. Bellini, A. Zavatta, G. Leuchs, C. Silberhorn, R. W. Boyd, L. L. Sánchez-Soto, A. Stefanov, M. Barbieri, A. Paterova, L. Krivitsky, S. Schwartz, K. Tamasaku, K. Dorfman, F. Schlawin, V. Sandoghdar, M. Raymer, A. Marcus, O. Varnavski, T. Goodson, Z. Zhou, B. Shi, S. Asban, M. Scully, G. Agarwal, T. Peng, A. V. Sokolov, Z. Zhang, M. S. Zubairy, I. A. Vartanyants, E. Del Valle, and F. Laussy, Roadmap on quantum light spectroscopy, *J. Phys. B: At. Mol. Opt. Phys.* **53**, 072002 (2020).
 - [39] J. Gea-Banacloche, Two-photon absorption of nonclassical light, *Phys. Rev. Lett.* **62**, 1603 (1989).
 - [40] B. Dayan, A. Pe’er, A. A. Friesem, and Y. Silberberg, Two photon absorption and coherent control with broadband down-converted light, *Phys. Rev. Lett.* **93**, 023005 (2004).

- [41] M. Richter and S. Mukamel, Collective two-particle resonances induced by photon entanglement, *Phys. Rev. A* **83**, 063805 (2011).
- [42] R. D. León-Montiel, J. Svozilík, J. P. Torres, and A. B. U'Ren, Temperature-controlled entangled-photon absorption spectroscopy, *Phys. Rev. Lett.* **123**, 023601 (2019).
- [43] J. Javanainen and P. L. Gould, Linear intensity dependence of a two-photon transition rate, *Phys. Rev. A* **41**, 5088 (1990).
- [44] F. Schlawin, K. E. Dorfman, and S. Mukamel, Entangled two-photon absorption spectroscopy, *Acc. Chem. Res.* **51**, 2207 (2018).
- [45] K. Matsuzaki and T. Tahara, Superresolution concentration measurement realized by sub-shot-noise absorption spectroscopy, *Nat. Commun.* **13**, 953 (2022).
- [46] F. Chen and S. Mukamel, Entangled two-photon absorption with Brownian-oscillator fluctuations, *J. Chem. Phys.* **156**, 074303 (2022).
- [47] A. Eshun, O. Varnavski, J. P. Villabona-Monsalve, R. K. Burdick, and T. Goodson III, Entangled photon spectroscopy, *Acc. Chem. Res.* **55**, 991 (2022).
- [48] B. E. A. Saleh, B. M. Jost, H. Fei, and M. C. Teich, Entangled-photon virtual-state spectroscopy, *Phys. Rev. Lett.* **80**, 3483 (1998).
- [49] A. Yabushita and T. Kobayashi, Spectroscopy by frequency-entangled photon pairs, *Phys. Rev. A* **69**, 013806 (2004).
- [50] S. Y. Baek and Y. H. Kim, Spectral properties of entangled photon pairs generated via frequency-degenerate type-I spontaneous parametric down-conversion, *Phys. Rev. A* **77**, 043807 (2008).
- [51] D. A. Kalashnikov, A. V. Paterova, S. P. Kulik, and L. A. Krivitsky, Infrared spectroscopy with visible light, *nat. Photon* **10**, 98 (2016).
- [52] M. Arahata, Y. Mukai, T. Tashima, R. Okamoto, and S. Takeuchi, Wavelength-tunable quantum absorption spectroscopy in the broadband midinfrared region, *Phys. Rev. Appl.* **18**, 034015 (2022).
- [53] P. G. Kwiat, K. Mattle, H. Weinfurter, A. Zeilinger, A. V. Sergienko, and Y. Shih, New high-intensity source of polarization-entangled photon pairs, *Phys. Rev. Lett.* **75**, 4337 (1995).
- [54] Y. Shih, Entangled biphoton source-property and preparation, *Rep. Prog. Phys.* **66**, 1009 (2003).
- [55] K. E. Dorfman, F. Schlawin, and S. Mukamel, Stimulated Raman spectroscopy with entangled light: enhanced resolution and pathway selection, *J. Phys. Chem. Lett.* **5**, 2843 (2014).
- [56] F. Schlawin, K. E. Dorfman, and S. Mukamel, Pump-probe spectroscopy using quantum light with two-photon coincidence detection, *Phys. Rev. A* **93**, 023807 (2016).
- [57] F. Chen and S. Mukamel, Vibrational hyper-Raman molecular spectroscopy with entangled photons, *ACS Photonics* **8**, 2722 (2021).
- [58] Z. Zhang, T. Peng, X. Nie, G. S. Agarwal, and M. O. Scully, Entangled photons enabled time-frequency-resolved coherent Raman spectroscopy and applications to electronic coherences at femtosecond scale, *Light Sci. Appl.* **11**, 274 (2022).
- [59] A. Ishizaki, Probing excited-state dynamics with quantum entangled photons: correspondence to coherent multidimensional spectroscopy, *J. Chem. Phys.* **153**, 051102 (2020).
- [60] Y. Fujihashi, K. Miwa, M. Higashi, and A. Ishizaki, Probing exciton dynamics with spectral selectivity through the use of quantum entangled photons, *J. Chem. Phys.* **159**, 114201 (2023).
- [61] D. A. Kalashnikov, E. V. Melik-Gaykazyan, A. A. Kalachev, Y. F. Yu, A. I. Kuznetsov, and L. A. Krivitsky, Quantum interference in the presence of a resonant medium, *Sci. Rep.* **7**, 11444 (2017).
- [62] Z. Sun, D. N. Basov, and M. M. Fogler, Graphene as a source of entangled plasmons, *Phys. Rev. Res.* **4**, 023208 (2022).
- [63] D. R. Baykusheva, M. H. Kalthoff, D. Hofmann, M. Claassen, D. M. Kennes, M. A. Sentef, and M. Mitrano, Witnessing nonequilibrium entanglement dynamics in a strongly correlated fermionic chain, *Phys. Rev. Lett.* **130**, 106902 (2023).
- [64] J. Hales, U. Bajpai, T. Liu, D. R. Baykusheva, M. Li, M. Mitrano, and Y. Wang, Witnessing light-driven entanglement using time-resolved resonant inelastic X-ray scattering, *Nat. Comm.* **14**, 3512 (2023).
- [65] G. Mazza and C. Budroni, Entanglement detection in quantum materials with competing orders, *Phys. Rev. B* **111**, L100302 (2025).
- [66] B. Kass, S. Talkington, A. Srivastava, and M. Claassen, Many-body photon blockade and quantum light generation from cavity quantum materials, *arXiv:2411.08964*.
- [67] D. N. Basov, A. Asenjo-Garcia, P. J. Schuck, X.-Y. Zhu, A. Rubio, A. Cavalleri, M. Delor, M. M. Fogler, and Mengkun Liu, Polaritonic quantum matter, *Nanophotonics*, 2025.
- [68] D. N. Basov, M. M. Fogler, and F. J. García de Abajo, Polaritons in van der Waals materials, *Science* **354**, aag1992 (2016).
- [69] K. Kakazu and Y. S. Kim, Quantization of electromagnetic fields in cavities and spontaneous emission, *Phys. Rev. A* **50**, 1830 (1994).
- [70] S. H. Abedinpour, M. Polini, A. H. MacDonald, B. Tanatar, M. P. Tosi, and G. Vignale, Theory of the pseudospin resonance in semiconductor bilayers, *Phys. Rev. Lett.* **99**, 206802 (2007).
- [71] P. Novelli, I. Torre, F. H. L. Koppens, F. Taddei, and M. Polini, Optical and plasmonic properties of twisted bilayer graphene: Impact of interlayer tunneling asymmetry and ground-state charge inhomogeneity, *Phys. Rev. B* **102**, 125403 (2020).
- [72] L. Cavicchi, K. J. A. Reijnders, M. I. Katsnelson, and M. Polini, Optical properties, plasmons, and orbital Skyrme textures in twisted TMDs, *arXiv:2410.18025*.
- [73] G. Grynberg, A. Aspect, and C. Fabre, *Introduction to Quantum Optics* (Cambridge University Press USA, New York, 2010).
- [74] R. Loudon, *The Quantum Theory of Light* (Oxford University Press Inc. USA, New York, 2000), 3rd Edition.
- [75] J. J. Hopfield, Theory of the contribution of excitons to the complex dielectric constant of crystals, *Phys. Rev.* **112**, 1555 (1958).
- [76] J. H. P. Colpa, Diagonalization of the quadratic boson Hamiltonian, *Phys. A: Stat. Mech. Appl.* **93**, 327 (1978).
- [77] C. K. Hong and L. Mandel, Theory of parametric frequency down conversion of light, *Phys. Rev. A* **31**, 2409 (1985).
- [78] A. Joobeur, B. E. A. Saleh, and M. C. Teich, Spatiotemporal coherence properties of entangled light beams generated by parametric down-conversion, *Phys. Rev. A* **50**,

- 3349 (1994).
- [79] C. K. Law, I. A. Walmsley, and J. H. Eberly, Continuous frequency entanglement: effective finite Hilbert space and entropy control, *Phys. Rev. Lett.* **84**, 5304 (2000).
 - [80] X. Ma and W. Rhodes, Multimode squeeze operators and squeezed states, *Phys. Rev. A* **41**, 4625 (1990).
 - [81] S. Dal Conte, C. Giannetti, G. Coslovich, F. Cilento, D. Bossini, T. Abebaw, F. Banfi, G. Ferrini, H. Eisaki, M. Greven, A. Damascelli, D. van der Marel, and F. Parmigiani, Disentangling the electronic and phononic glue in a high- T_c superconductor, *Science* **335**, 1600 (2012).
 - [82] D. Brida, A. Tomadin, C. Manzoni, Y. J. Kim, A. Lombardo, S. Milana, R. R. Nair, K. S. Novoselov, A. C. Ferrari, G. Cerullo, and M. Polini, Ultrafast collinear scattering and carrier multiplication in graphene, *Nat. Commun.* **4**, 1987 (2013).
 - [83] A. Tomadin, D. Brida, G. Cerullo, A. C. Ferrari, and M. Polini, Nonequilibrium dynamics of photoexcited electrons in graphene: Collinear scattering, Auger processes, and the impact of screening, *Phys. Rev. B* **88**, 035430 (2013).
 - [84] G. Mazza, M. Gandolfi, M. Capone, F. Banfi, and C. Giannetti, Thermal dynamics and electronic temperature waves in layered correlated materials, *Nat. Comm.* **12**, 6904 (2021).
 - [85] R. Mankowsky, A. Subedi, M. Först, S. O. Mariager, M. Chollet, H. T. Lemke, J. S. Robinson, J. M. Glownia, M. P. Minitti, A. Frano, M. Fechner, N. A. Spaldin, T. Loew, B. Keimer, A. Georges, and A. Cavalleri, Nonlinear lattice dynamics as a basis for enhanced superconductivity in $\text{YBa}_2\text{Cu}_3\text{O}_{6.5}$, *Nature* **516**, 71 (2014).
 - [86] For a recent review see e.g. A. S. Disa, T. F. Nova, and A. Cavalleri, Engineering crystal structures with light, *Nat. Phys.* **17**, 1087 (2021).
 - [87] J. Rammer, *Quantum Field Theory of Non-equilibrium States* (Cambridge University Press, Cambridge, 2007).
 - [88] R. J. Glauber, The quantum theory of optical coherence, *Phys. Rev.* **130**, 2529 (1963).
 - [89] M. E. Siemens, Q. Li, R. Yang, K. A. Nelson, E. H. Anderson, M. M. Murnane, and H. C. Kapteyn, Quasi-ballistic thermal transport from nanoscale interfaces observed using ultrafast coherent soft X-ray beams, *Nat. Mater.* **9**, 26 (2010).
 - [90] F. Campaioli, S. Gherardini, J. Q. Quach, M. Polini, and G. M. Andolina, Colloquium: Quantum batteries, *Rev. Mod. Phys.* **96**, 031001 (2024).
 - [91] I. S. Gradshteyn, and I. M. Ryzhik, *Table of Integrals, Series, and Products*, A. Jeffrey and D. Zwillinger, (Elsevier Academic Press, Amsterdam, 2007), 7th Edition, Translated from Russian by Scripta Technica, Inc.